Advanced Science

S, N-co-doped Graphene-Nickel Cobalt Sulfide Aerogel: Improved Energy Storage and Electrocatalytic Performance

--Manuscript Draft--

Manuscript Number:	advs.201600214R1
Full Title:	S, N-co-doped Graphene-Nickel Cobalt Sulfide Aerogel: Improved Energy Storage and Electrocatalytic Performance
Article Type:	Full Paper
Section/Category:	Physical Sciences and Engineering
Keywords:	Aerogel, nickel cobalt sulfide, rechargeable alkaline battery, oxygen reduction reaction
Corresponding Author:	Ivan P. Parkin, Prof. University College London London, UNITED KINGDOM
Corresponding Author Secondary Information:	
Corresponding Author's Institution:	University College London
Corresponding Author's Secondary Institution:	
First Author:	Guanjie He
First Author Secondary Information:	
Order of Authors:	Guanjie He
	Mo Qiao
	Wenyao Li
	Yao Lu
	Tingting Zhao
	Rujia Zou
	Bo Li
	Jawwad A. Darr
	Maria-Magdalena Titirici
	Ivan P. Parkin, Prof.
Order of Authors Secondary Information:	
Abstract:	Metal sulfides are commonly used in energy storage and electrocatalysts due to their redox centres and active sites. Most literature reports show that their performance decreases significantly caused by oxidation in alkaline electrolyte during electrochemical testing. Herein, S and N co-doped graphene-based nickel cobalt sulfide aerogels were synthesized for use as rechargeable alkaline battery electrodes and oxygen reduction reaction (ORR) catalysts. Notably, our system shows improved cyclability due to the stabilization effect of the S and N co-doped graphene aerogel (SNGA). This reduces the rate of oxidation and the decay of electronic conductivity of the metal sulfides materials in alkaline electrolyte, i.e. the capacity decrease of CoNi2S4/S, N-co-doped graphene aerogels (CoNi2S4/SNGA) was 4.2 % for 10000 cycles in a three electrode test; the current retention of 88.6 % for Co-S/S, N-co-doped graphene aerogels (Co-S/SNGA) after 12000s current-time chronoamperometric response in the ORR test is higher than corresponding Co-S nanoparticles and Co-S/non-doped graphene aerogels. Importantly, our results confirmed that the Ni-Co-S ternary materials behaved as an electrode for rechargeable alkaline batteries rather than supercapacitors electrodes in three electrode test as commonly described and accepted in the literature. Furthermore, we specified formulas to evaluate the

	performance of hybrid battery devices.
Additional Information:	
Question	**Response**
Please submit a plain text version of your cover letter here. Please note, if you are submitting a revision of your manuscript, there is an opportunity for you to provide your responses to the reviewers later; please do not add them to the cover letter.	Dear Editor and Referees, Please find attached our manuscript entitled “S, N-co-doped Graphene-Nickel Cobalt Sulfide Aerogel: Improved Energy Storage and Electrocatalytic Performance.” On behalf and with the full approval of my fellow co-authors Guanjie He, Mo Qiao, Wenyao Li, Yao Lu, Tingting Zhao, Rujia Zou, Bo Li, Jawwad A. Darr, Junqing Hu and Maria-Magdalena Titirici. I am submitting this manuscript to the Advanced Science for publication as a Full paper. This manuscript has not been published previously, and is not under consideration for publication in another journal at this time. This paper reports the first use of S and N co-doped graphene-based nickel cobalt sulfide aerogels as rechargeable alkaline battery electrodes and oxygen reduction reaction catalysts. We dramatically improved the electrochemical performances by managing to overcome the problems associated with aggregation of graphene materials and rapid performances decline of metal sulfides materials due to oxidation in alkaline electrolyte and electronic conductivity decline during long-term cycling. Importantly, from a kinetic viewpoint, we described the use of nickel cobalt sulfide materials in alkaline electrolyte for energy storage testing system as the rechargeable alkaline battery electrodes. We further provided detailed caculation fomula to illustrate the performances of hybrid battery (e.g. energy density and the maximun output power density). The formulas in our paper were more accurate and understandable than commonly used supercapacitors equations to evaluate these devices. As suggested by editor from other wiley journal and comments from referees, we have modified the manuscript and planned to submit to Advanced Science. The relevance of this work to nanostructure synthesis, well-defined concept as well as excellent performances for energy storage and electrocatalysis is likely to appeal to the broad readership of Advanced Science. We would be grateful if the manuscript could be reviewed and considered for publication on Advanced Science. Sincere yours, Ivan P. Parkin Professor 20 Gordon Street, London, U.K. Head of Department, Department of Chemistry WC1H 0AJ University College London E-mail:i.p.parkin@ucl.ac.uk

WILEY-VCH

DOI: 10.1002/ ((please add manuscript number))
Article type: Full Paper

S, N-co-doped Graphene-Nickel Cobalt Sulfide Aerogel: Improved Energy Storage and Electrocatalytic Performance

*Guanjie He[a], Mo Qiao[b], Wenyao Li[c], Yao Lu[a], Tingting Zhao[a], Rujia Zou[c], Bo Li[d], Jawwad A. Darr[a], Junqing Hu[c], Maria-Magdalena Titirici[b] and Ivan P. Parkin[a]**

Guanjie He, Yao Lu, Tingting Zhao, Prof. Jawwad A. Darr, Prof. Ivan P. Parkin

[a]Christopher Ingold Laboratory, Department of Chemistry, University College London, 20 Gordon Street, London WC1H 0AJ, U.K.,

E-mail:i.p.parkin@ucl.ac.uk

Mo Qiao, Prof. Maria-Magdalena Titirici

[b]School of Engineering and Materials Science/Materials Research Institute, Queen Mary University of London, Mile End Road, E14NS, London, UK.

Dr. Wenyao Li, Prof. Rujia Zou, Dr. Bo Li, Prof. Junqing Hu

[c]State Key Laboratory for Modification of Chemical Fibers and Polymer Materials, College of Materials Science and Engineering, Donghua University, Shanghai 201620, China.

Keywords: Aerogel, nickel cobalt sulfide, rechargeable alkaline battery, oxygen reduction reaction

Abstract: Metal sulfides are commonly used in energy storage and electrocatalysts due to their redox centres and active sites. Most literature reports show that their performance decreases significantly caused by oxidation in alkaline electrolyte during electrochemical testing. Herein, S and N co-doped graphene-based nickel cobalt sulfide aerogels were synthesized for use as rechargeable alkaline battery electrodes and oxygen reduction reaction (ORR) catalysts. Notably, our system shows improved cyclability due to the stabilization effect of the S and N co-doped graphene aerogel (SNGA). This reduces the rate of oxidation and the decay of electronic conductivity of the metal sulfides materials in alkaline electrolyte,

i.e. the capacity decrease of $CoNi_2S_4$/S, N-co-doped graphene aerogels ($CoNi_2S_4$/SNGA) was 4.2 % for 10000 cycles in a three electrode test; the current retention of 88.6 % for Co-S/S, N-co-doped graphene aerogels (Co-S/SNGA) after 12000s current-time chronoamperometric response in the ORR test is higher than corresponding Co-S nanoparticles and Co-S/non-doped graphene aerogels. Importantly, our results confirmed that the Ni-Co-S ternary materials behaved as an electrode for rechargeable alkaline batteries rather than supercapacitors electrodes in three electrode test as commonly described and accepted in the literature. Furthermore, we specified formulas to evaluate the performance of hybrid battery devices.

Main text

Graphene has attracted great research interest after its first discovery in 2004.[1] With two dimensional layered structure of carbon atoms, graphene possesses unique properties, such as high theoretical surface area (2630 m^2 g^{-1}),[2] thermal and chemical stability,[3] remarkable electronic and mechanical properties,[4, 5] *etc.* Nevertheless, due to the strong van deer Waals forces among the single carbon sheets, graphene has the tendancy to aggregate and form graphite,[6] which leads to a sharp decrease in surface area and kinetic ion transport, affecting the performance of these materials when used in energy storage[4] and electrocatalysis[7]. In order to solve the aggregation problem and achieve fast ion and electron transfer, novel graphene structures have been developed. Reports include graphene foams prepared by template-assisted chemical vapour deposition (CVD) methods[8], self-assembly of aerosol or hydrogel by hydrothermal processes[9, 10] or electrospray ionization[11] and layer-by-layer composite structures by filter assembly[6, 12]. However, carbon materials alone, suffer from low charge storage capacity and limited active sites[3, 13, 14], which hinder their use as high performance energy storage devices and electrocatalysts.

One effective way to improve the performance of graphene materials, expand and improve their applications is to hybridize them with metal-based semiconductors to form nanocomposites[15]. Recently, nickel cobalt-based oxides, sulfides and selenides have been successfully used as the non-noble metal cadidates in various electrochemical applications, such as Li-ion batteries[16, 17], supercapacitors[6, 18-22] and eletrocatalysts[23-25]. Various nanostructures have been designed and synthesized, such as nanosheets[26, 27], nanorods[16], self-assembled nanoflowers[18], core-shell structures[28], mesoporous structures and dendritic structures[29], *etc*. For instance, Lou *et al.* have fabricated nickel cobalt sulfide ball-in-ball hollow spheres *via* an anion exchange method and used them as supercapacitor electrodes[28], delivering a specific capacitance of 1036 F g^{-1} at a current density of 1 A g^{-1} and retaining 87 % of its initial specific capacitance after 2000 cycles. Dai *et al.* synthesized $Co_{1-x}S$/reduced graphene oxide hybrid catalysts showing a high ORR current density of 1.1 mA cm^{-2} at 0.7 V *vs.* RHE with ~100 μg cm^{-2} loading density.[30] Compared with transitional metal oxides, transitional metal sulfides or selenides usually possess better electron conductivity[31-33]. Taking into account their price, performance stabilities and safety issues, metal sulfides are very attractive for electrochemical applications. The main hurdle to their use is their easy oxidization in alkaline electrolytes and the decay of electron conductivity especially during long term cycles.[34] To address this problem, it is important to develop innovative Ni-Co-S nanostructures with improved stability and performances.

On the basis of the above idea, we designed and synthesized N, S co-doped (S-rich) graphene-based nickel cobalt sulfide aerogels (Ni-Co-S/SNGA) with the aim to optimize the performances of metal sulfides, in particlar their cycling performance and illustrate their potential widespread application. The Ni-Co-S/SNGA exhibited improved electrochemical performance as electrodes for rechargeable alkaline batteries and as electrocatalysts for ORR in alkaline electrolyte.

The main synthetic procedure to prepare Ni-Co-S/SNGA is illustrated by Figure 1a. Four different Ni-Co-S nanostructures (*i.e.* $CoNi_2S_4$, $NiCo_2S_4$, Ni-S and Co-S) were prepared by one-step hydrothermal process with different precursor ratios. The materials were freeze-dried before use. Graphene oxide (GO) was prepared by a modified Hummer method[12] from graphite powders. Various hybrid materials were produced from mixtures of specific ratios of GO water solutions, thiourea (S and N source) and Ni-Co-S nanostructures in an autoclave at 180 ºC for 12 h followed by a three-day freeze-drying process. Nitrogen doped graphene provides enhanced electron conductivity and ion electroactivity to materials. This is ascribed to the lone electron pairs from the nitrogen atoms forming delocalized conjugated systems with the sp^2-hybridized carbon frameworks.[35] Sulfur doping was suggested to expand the highly efficient space utilization of carbon materials and improve the energy storage performances.[36] The sulfur atoms are covalently incorporated into graphene and facilitated the bridging of metal sulfides materials to the graphene frameworks, thus enabling improved robustness of the composite materials.[37] In addition, thiourea can not only support N and S co-doping but also reduce the graphene oxide under the hydrothermal process thus further improving the electron conductivity. The digital camera pictures of the typical samples are shown in Figure. 1b. Moreover, the as-synthesized samples are superhydrophilic. The measured contact angle of a water droplet on the hybrid aerogel is 0° showing that it is fully wetted which is a highly beneficial characteristic for electrochemical reactions in aqueous electrolytes.

The morphologies of these materials were investigated by scanning electron microscopy (SEM). From the low-magnification SEM images (Figure. S1), it can be observed that the Ni-Co-S nanoparticles were distributed uniformly on the surface of the porous graphene nanosheets. Porous channels can be observed for all four types of Ni-Co-S/SNGA. From the

high-magnification images (Figure. 2), the Ni-Co-S nanoparticles size could be determined. These particles were several tens of nanometers to hundreds of nanometers in size with a rounded particle shape or a nanorod shape within larger nanocluster structures. The small primary particle size together with the large surface contact area with the electrolyte is expected to accelerate the rate of redox reaction or catalytic actions.

The crystallographic phases of the four types of Ni-Co-S nanostructures/SNGA were further characterized by powder X-ray diffraction (XRD). Figure. 3a shows the XRD pattern of the $CoNi_2S_4$/SNGA samples, which correspond to the standard $CoNi_2S_4$ Fd-3m crystal structures (JCPDS no. 24-0334). XRD patterns of $NiCo_2S_4$/SNGA, Ni-S/SNGA and Co-S/SNGA samples are shown in Figure. S2(b-d), the peaks of which can be indexed to the standard diffraction patterns. The weak peaks at ~ 24^o in 2θ can be assigned as the (002) plane of SNGA. Figure. 3b shows that the hydrothermally obtained $CoNi_2S_4$ nanostructures maintained a uniform urchin-like morphology with nanorods self-assembled radially and grown from the centre, forming $CoNi_2S_4$ nanoclusters and capped by the graphene aerogel (GA), illustrated in Figure. 2b. The individual nanorods have the diameter of ~ 15 nm (Figure. 3c). HRTEM image of $CoNi_2S_4$/SNGA in Figure. 3d showed clear lattice fringes with d-spacing of 0.54 nm which can be indexed to the (111) plane of the Fd-3m crystal structures of $CoNi_2S_4$, in accordance with the XRD results.

Raman spectroscopy was performed to confirm the graphitization and composition of the GO, $CoNi_2S_4$/GA, $CoNi_2S_4$/S, N co-doped graphene hybrid materials ($CoNi_2S_4$/SnrGO, Figure. S3) and $CoNi_2S_4$/SNGA samples, respectively. The two sharp peaks at 1353.2 and 1591.3 cm^{-1} correspond to the D and G peaks of GO and SNGA from the nanocomposites. The I(D)/I(G) value of the GO aerogel varied with the composition of the $CoNi_2S_4$ nanostructures and S, N co-doping indicated that the degree of graphitization decreased with doping although the GO

aerogel reduced to graphene.[10]. Among four different composition materials, $CoNi_2S_4$/SNGA possessed the highest I(D)/I(G) value (Table. S1), which proved that this sample has the highest reduction degree of GO which will produce more defects structures among graphene sheets than the other samples[35]. The nature of the surface functionalities, along with the distributions of their valance states were analyzed by SEM-EDS mapping (Figure. S4) and X-ray photoelectron spectroscopy (XPS). The sulphur was densely distributed within the structures, which demonstrated the S-rich nature of the as-synthesized samples. Figure. 4b shows the fitted C 1s peak of the XPS spectrum. The sharp peak at 284.4 eV was indexed to the sp^2 C=C graphite bond. The peak at 285.6 eV was attributed to C-S and C=N bonding, indicating S and N co-doped graphene and consistent with the FT-IR spettrum (Figure. S5). The weaker 288.3 eV peak is due to defects and functional groups including C-N, C-O and O-C-O,[39] the defect structures among graphene sheets can be directly related to the Raman results. The high resolution N 1s spectrum is shown in Figure. 4c, and can be deconvoluted into three separated peaks: pyridinic N (398.1 eV), pyrrolic N (399.9 eV) and graphitic N (401.7 eV), respectively.[40] The spectra of Ni 2p and Co 2p are shown in Figure. 4d and 4e, and both of the Ni and Co elements can be fitted with two spin orbit doublets and two shake-up satellites. The doublets containing the low energy bands (Ni 2p3/2 and Co 2p3/2) and the high energy bands (Ni 2p1/2 and Co 2p1/2) respectively. This represented both the divalent and trivalent states of Ni and Co in the samples.[16, 19] The S 2p spectrum (Figure. 4f) can be divided into two main peaks located at ~ 162.0 and 163.2 eV and one shake-up satellite at ~ 169.0 eV. The component at 163.2 eV corresponded to metal-sulfur bonds, and the peak at 162.0 eV can be attributed to the sulfur ions at low coordination numbers on the surface.[41, 42] From XPS results of SNGA, the atom ratio of C 1s, S 2p and N 1s are 88.76 %, 4.76 % and 6.48 %, respectively.

To explore the electrochemical performance of the as-synthesized electrodes, we carried out cyclic voltammetry (CV) and galvanostatic charge-discharge (GCD) measurements on the as-synthesized materials by pressing them directly into Ni foams as the working electrode without adding any conductive agents and binders in a three-electrode test system with 6 M KOH as the electrolyte. We investigated the optimized performance of the samples by changing the ratio of nanoparticles to SNGA. From Figure. 5a, the specific capacity values of $CoNi_2S_4$/SNGA, $NiCo_2S_4$/SNGA, Ni-S/SNGA and Co-S/SNGA were 192.1, 190.9, 167.5 and 184.0 mAh g^{-1} respectively at a current density of 10 A g^{-1}. The rate capabilities of those samples remained ~ 44 % of the original values, when the current density was increased by 30 times, as shown in Figure. S7c. The excellent specific capacity values and rate capabilities demonstrated the applicability of this rational design whereby different Ni-Co-S nanoparticles were investigated. The best performing material among the four tested as electrodes is the $CoNi_2S_4$/SNGA and the similar value can be seen from $NiCo_2S_4$/SNGA. This can be explained as the richer redox centres and the synergistic effect of both nickel and cobalt ions in the sulfides (redox reactions 1, 2 and 3). Figure. 5b shows the CV curves of $CoNi_2S_4$/SNGA electrodes within the voltage range -0.1 to 0.4 V (*vs.* Ag/AgCl) at scan rates ranging from 1 to 50 mV s^{-1}.

As clarified by Dunn. *et al*[43], if a redox reaction is limited by semi-infinite diffusion like the battery type, the peak current I varies as $V^{1/2}$; for a capacitive process, it varies as V. This relation is expressed as $I = aV^b$, with the value of b providing insight regarding the charge storage mechanism. In our system, the pairs of well-defined redox peaks can be detected in all CV curves. The fitted value of b = 0.65 for the anodic peak current and b = 0.58 for cathodic peak current, the peak current I closely varies as $V^{1/2}$ (sweep rate) (detailed plot in Figure. S8), indicating these redox reactions are semi-infinite diffusion. From the curves in Figure. 5b, it can be observed that the anodic peaks shift towards positive potentials while the cathodic

peaks shifts towards negative potentials, respectively. The reaction is limited by the charge transfer kinetics. Increasing the scan rate, the redox peaks become obvious and only one pair of redox peaks can be observed in the curves (scan rate of 40 and 50 mV s^{-1}), which can be explained as the polarization of the electrode at a high scan rate. These distinct peaks can be attributed to the reversible Faradaic redox processes of Ni^{2+}/Ni^{3+} and $Co^{2+}/Co^{3+}/Co^{4+}$ redox couples based on the following reactions:

$$NiS + OH^- \rightleftarrows NiSOH + e^- \quad (1)$$

$$CoS + OH^- \rightleftarrows CoSOH + e^- \quad (2)$$

$$CoSOH + OH^- \rightleftarrows CoSO + H_2O + e^- \quad (3)$$

Because of these types of reversible redox reactions, we defined these materials in this reaction system for energy conversion and storage as rechargeable alkaline battery electrodes. *Ex-situ* XRD measurements (Figure. S9) of $CoNi_2S_4$/SNGA samples during different electrochemical steps were carried out. The change in reflections implied the phase changing during this process and confirmed that redox reactions are occurring in bulk, further demonstrating the alkaline battery reactions.

GCD performances for the various synthesized Ni-Co-S/SNGA samples were conducted in the voltage ranges of -0.1 to 0.35 V (*vs.* Ag/AgCl). The intrinsic properties of the CV curves (Figure. 5b and Figure. S7a) and voltage plateaus observed during discharge curves (Figure. 5a and Figure. S6) demonstrated obvious kinetic information so that these materials can be defined as rechargeable alkaline batteries electrodes, contrary to the previously reported materials which were classified as pseudocapacitor electrodes.[6, 19, 26, 28, 29, 42, 44] The narrower voltage range of GCD compared with the CV curves is due to the fact that the electrode is not fully charged at low current densities (*e.g.* 1 A g^{-1}). Therefore, the specific capacity values of the materials presented here are slightly lower compared to those recorded at a larger voltage range (see Figure. S10 and the calculation of specific capacity for $CoNi_2S_4$/SNGA at 20 A g^{-1}

under different voltage ranges). When using different $CoNi_2S_4$ nanoparticles and SNGA ratios, *i.e.* 0.14 g of nanoparticles in 70 mg of GO precursors (2:1 $CoNi_2S_4$/SNGA), a high specific capacity and rate capacity was achieved compared with other ratios tested. The specific capacity was 318.3, 281.3, 226.5, 192.1, 161.1 and 141.2 mAh g^{-1} at current densities of 1, 2, 5, 10, 20, 30 A g^{-1}, respectively. The rate capability was ~ 44.3 % when the current density was increased 30 times. The best performance of the 2:1 $CoNi_2S_4$/SNGA is as the result of an optimum ratio of active materials and porosity. Therefore, all of the other experiments were conducted using this ratio unless stated otherwise. Compared with the $CoNi_2S_4$ nanoclusters and the same ratio $CoNi_2S_4$/GA, 1:1 and 3:1 $CoNi_2S_4$/SNGA samples exhibited higher specific capacity at all current densities.

The electronic conductivities of $CoNi_2S_4$/SNGA, $CoNi_2S_4$/GA and $CoNi_2S_4$ nanoclusters are significant parameters and can be used to explain the differences in performances between the various materials. Electrochemical impedance spectra (EIS) were employed as depicted in Figure. 5d. The Nyquist plots had a semicircle in the high-to-medium frequency region (inset in Figure. 5d) and a slope in the low frequency region. The semicircle is attributed to charge transfer processes at the electrode/electrolyte interface, while the plot corresponds to electrolyte diffusion processes into the bulk of the electrode, *i.e.* Warburg diffusion.[44, 45] In the case of $CoNi_2S_4$/SNGA material, the slope was more abrupt indicating that the Warburg resistance (Zw, diffusive impedance of the OH^- ion) appears not to be the determining factor. This material can therefore store charge more efficiently when used as an electrode.

Figure. S11 shows the modified equivalent circuit model of our system, the equivalent series resistance (Rs) values, including inherent resistances of the active materials, bulk resistance of electrolyte and contact resistance of the interface between electrolyte and electrodes. The Rs values were 0.155, 0.192 and 0.185 Ω for $CoNi_2S_4$/SNGA, $CoNi_2S_4$/GA and $CoNi_2S_4$

nanoclusters, respectively (Well-fitted EIS spectra were shown in Figure. S12). The relatively low values are similar for all three samples, which suggest the spinel structures of $CoNi_2S_4$ nanoparticles could possess metallic electronic conductivity.[31] GA with the lower reduction degree of GO could result in a decline of the conductivity of the whole structure. The charge-transfer resistance (Rct) values, calculated from the semi-circle in the high-frequency region, reflect the diffusion of electrons, and are 0.43, 2.02 and 1.37 Ω for $CoNi_2S_4$/SNGA, $CoNi_2S_4$/GA and $CoNi_2S_4$ nanoclusters, respectively. The lower capacity value of $CoNi_2S_4$ powder samples can be explained by the electrode manufacture procedure (without adding binder), which can lead to leakage and aggregation of the materials that were immersed into the electrolyte especially under the working state. The $CoNi_2S_4$/SNGA system possessed the smallest resistance among its other counterparts, its electronic conductivity is the determining factor for the high-performance rechargeable alkaline battery electrode.

Lou *et al.* reported that the surface of metal sulfides can be electrochemically transformed to metal hydroxides upon repeated cycling processes.[28] Indeed, the biggest challenge related to metal sulfides materials when used in energy storage is their unsatisfactory cyclability, due to the oxidation of sulfide materials and the decline of conductivity especially after long-term cycling. Here, we have conducted long term cyclic GCD tests of 10000 cycles for the as-synthesized $CoNi_2S_4$/SNGA at a current density of 10 A g^{-1}. The specific capacity of the 10000^{th} cycle was ~ 95.8 % of its 1^{st} cycle value. The Coulombic efficiency of the sample stayed at ~ 100 % except for the first few cycles, meaning an excellent reversible redox process. $CoNi_2S_4$/SNGA samples in our work for the three electrode test proved to have superior specific capacity and cycling performances among the most of the reported for nickel/cobalt sulfide materials (See Table. S2 for comparison). For comparison, the specific capacity value of the 3000^{th} cycle of $CoNi_2S_4$/GA, $CoNi_2S_4$/NGA and $CoNi_2S_4$/SGA was ~ 85.1 %, 77% and 93 % of its initial value under the same test conditions; moreover, the S

element signal in XPS for $CoNi_2S_4$/GA and $CoNi_2S_4$/NGA could hardly be detected (Figure. S13 and Figure. S14d). The specific capacity value of the 3000th cycle for $CoNi_2S_4$ powdery sample was ~ 76.5 % of its initial values after cycling. The TEM mapping images (Figure. S15) and XPS data (Figure. S16) after cycling confirmed the composition and structure stability of the $CoNi_2S_4$/SNGA samples. Sulfur and nitrogen can also be detected from the elemental mapping images from the TEM and metal-sulfide binding can be inferred from the XPS data, which indicates that the $CoNi_2S_4$/SNGA structure is very stable and can slow down the electrochemical transformation of the metal sulfides to metal hydroxides. The morphology of $CoNi_2S_4$ nanorods became rough (TEM image in inset of Figure. 5e) due to the long time electrochemical reactions. However the $CoNi_2S_4$ nanostructures were still capped in the initial SNGA structures. The impedance spectra (Figure. S17) after the cycling showed the Rs and Rct are 0.294 and 1.85 Ω, respectively, which increased fractionally compared with their initial values, and have comparable or slightly smaller values compared with the reported similar binder-free metal sulfide materials before cycling.[19, 44, 46] Similar cycling performances can also be observed for $NiCo_2S_4$/SNGA, Ni-S/SNGA and Co-S/SNGA samples. The 3000th cycles of all these four samples possessed capacity retention higher than *ca.* 89 % (Figure. S7d). Moreover, the specific capability and low resistance (Figure. S7b, c) indicate these Ni-Co-S/SNGA possess high performance. By Comparing the electrochemical performances of these samples, the functions of S and N doping can be clarified. Nitrogen doping could be used to improve the electron conductivity and ion electroactivity of the graphene aerogel and sulfur doping can help stabilize the metal sulfides. These evidences proved the general usability of this structure to improve the performances of the Ni-Co-S materials used for rechargeable alkaline batteries electrodes, especially the cycling performances.

In order to evaluate the $CoNi_2S_4$/SNGA electrode for practical applications, a solid-state

hybrid battery was fabricated by using the $CoNi_2S_4$/SNGA pressed into nickel foam as the positive electrode, the SNGA pressed into nickel foam as the negative electrode, 2 M KOH-PVA solution as the gel electrolyte and commercial glassy fiber paper as the separator. Solid-state hybrid battery has similar structures as reported previously to so-called asymmetric supercapacitors. The electrochemical reactions at the anode was as stated by reactions 1-3. The negative electrode is a graphene aerogel based electrical double layer capacitor (EDLC), it has the mechanism of electrostatic adsorption for energy storage at the interface of the electrodes. The device is based on the electrodes of rechargeable alkaline battery and EDLC, we defined it as a hybrid battery, as they possess obvious redox peaks with semi-infinite diffusion reactions. Figure. 6a displays the CV curves of the solid-state hybrid battery (SNGA//$CoNi_2S_4$/SNGA) at various scan rates (10~200 mV s^{-1}) in the voltage range of 0~1.6 V. Clearly, the CV curves showed hybrid capacity of both an electric double-layer capacitor and a redox reaction of a battery. The volumetric specific capacity of the devices was calculated from the GCD curves (Figure. 6b). The fabricated SNGA//$CoNi_2S_4$/SNGA device processed the volumetric specific capacity of 2.37, 1.99, 1.49, 1.24, 1.14, 0.92 and 0.76 mAh cm^{-3} at current densities of 1, 2, 5, 8, 10 and 20 mA cm^{-2}, respectively. From the discharge curve, it possess unconspicuous voltage plateaus indicating the pseudocapacitor-like hybrid feature. Energy density and power density are two key metrics for evaluating the performances of the energy storage device. Figure. 6c shows the plots of power density *vs.* energy density (Ragone plot) of the solid-state hybrid battery on the basis of the total volume of the device. The volumetric energy density and power density of the hybrid battery were calculated according to the well-defined equations in the Supporting information (equation 4-10). The device exhibited a high volumetric power density (maximum output value) of 17.5 W cm^{-3} while retaining its high energy density of 1.95 mWh cm^{-3} at a current of 1 mA. This value remained almost constant with increasing current, which is comparable or better than most of the reported symmetric or asymmetric devices (SDs or ADs)[47] based on the

volumetric density, such as ZnO@C@MnO_2-SDs[48], TiO_2@C-SDs[49], WO_{3-x}/MoO_{3-x}//PANI/carbon fabric-Ads[50], H-TiO_2@MnO_2//H-TiO_2@C-ADs[51], laser-scribed graphene SDs[52], MnO_2//Fe_2O_3 ADs[53], Co_9S_8//Co_3O_4@RuO_2-ADs[54] and ZnO@MnO_2//RGO-ADs[55]. The energy density and power density based on the total mass of the hybrid battery are shown in Figure. S19. The high power density value was retained showing a superior behaviour to some of the literature reported hybrid devices based only on the caculation of the active materials[56, 57]. The cycling performances for the hybrid battery are shown in Figure. 6d at a current of 20 mA. It manifested a high cycling stability and overall capacity decrease of only ~ 0.002 % per cycle within 8000 cycles. The Coulumbic efficiency of the hybrid battery stayed at ~ 100 %. The cycling performances are better than or comparable to the similar PVA gel electrolyte based solid-state devices (Table. S3 for comparison). Moreover, with the new gel electrolyte dropping on the solid-state hybrid battery, the capacity increased dramatically with several hundreds of cycles increasing together with the internal resistance change (Figure. S20), indicating the main reason for the decline in performance is further water evaporation in the gel electrolyte thus causing the internal resistor to increase and limiting the contacting reaction sites with the active materials.

Ni-Co-S ternary systems can also be used as electrocatalysis as they have noble-metal like catalytic properties, while their stability should be influenced when used in an alkaline electrolyte especially in O_2 saturated KOH. Thus we have also explored the use of Ni-Co-S/SNGA materials as ORR catalysts. Figure. 7a shows the CV of Ni-Co-S/SNGA in O_2-saturated 0.1 M KOH at room temperature. The peak potential of Co-S/SNGA nanostructures (0.75 V *vs.* RHE) is more positive than other Ni-Co-S/SNGA nanostructures, with similar values of $NiCo_2S_4$/SNGA (0.746 V *vs.* RHE). The ORR performances of the four materials evaluated based on Ni-Co-S/SNGA nanostructures were further compared by rotating-disk electrode (RDE) measurement in O_2-saturated 0.1 M KOH at 1600 rpm with a sweep rate of

10 mV s^{-1}, as shown in Figure. 7b and Figure. S21a. The Co-S/SNGA nanostructure showed the best performance compared with other Ni-Co-S/SNGA nanostructures, Co-S nanoparticles and Co-S/GA, with the onset potential of 1.0 V *vs*. RHE and limiting current density of 4.6 mA cm^{-2}. As reported, with the increase of Ni^{3+} parts in Ni-Co-S, the ORR catalysts show poorer performance.[58] The electron transfer number of Co-S/SNGA ranged from 3.8~3.95 during the voltage range of 0.2~0.8 *vs.* RHE, revealing the four-electron pathway reaction. Similar results can be seen from $NiCo_2S_4$/SNGA from Figure. S21b, while the electron transfer number remained stable at 3.8~3.95, indicating a four-electron pathway of this sample. The $CoNi_2S_4$/SNGA material also showed a four-electron type reaction while the Ni-S/SNGA showed a mixed two- and four-electron hybrid pathway. With an increase of Ni ion in the hybrid structures, the ORR performance decreased. Moreover, from the comparison experiments (Figure. S22), the oxygen reduction reaction (ORR) performances of $NiCo_2S_4$/SNrGO are similar to that of $NiCo_2S_4$/SNGA, which indicates that the aerogel structures has almost no influence on the interaction of each component.

Stability is another important index to evaluate the performance of ORR catalysts. As expected, the SNGA wrapped Co-S nanostructures showed better performance, and maintained ~ 88.6 % of the initial value after 12000 s of current-time chronoamperometric responses at a rotation rate of 1600 rpm in O_2-saturated 0.1 M KOH, higher than Co-S nanoparticles and Co-S/GA. The usability of these structures can also be evidenced by $NiCo_2S_4$/SNGA, with the ~ 91.5 % retention (Figure. S23) after 12000 s in the current-time chronoamperometric responses.

In summary, we have developed Ni-Co-S/SNGA materials as a viable alternative to the existing materials to improve the electrochemical performances especially the cycling

performances of Ni-Co-S ternary metal sulfide materials both for rechargeable alkaline battery electrodes and ORR catalysts. The $CoNi_2S_4$/SNGA samples showed the best performance, which delivered a high specific discharge capacity of 318.3 mAh g^{-1} at 1 A g^{-1}. The capacity can retain 44.3 % of the initial value when the current density increased 30 times. The capacity retention of ~ 95.8 % of the initial specific capacity after a long GCD cycle of 10000. The high-rate hybrid battery based on $CoNi_2S_4$/SNGA as the positive electrode and SNGA as the negative electrode delivered a high volumetric power density of 17.5 W cm^{-3} while it retained its high volumetric enegy density of 1.95 mWh cm^{-3} at the current of 1 mA. The hybrid battery showed an excellent cycling performance and the capacity decrease was only ~ 0.002 % per cycle within 8000 cycles. When used as electrocatalysts in ORR, it was observed that an increase of Ni ion in the hybrid structures decreased the performance. Remarkably, SNGA structures capped with metal sulfide represent enhanced stability for ORR. Moreover, we confirmed the commonly regarded supercapacitor electrodes based on Ni-Co-S ternary materials as electrode in rechargeable alkaline batteries from a kinetic view. We have also proposed accurate caculation formulas to evaluate the performance of the hybrid battery devices, which could serve as a standardization for performance comparisons in future work for hybrid batteries.

The excellent performance of our materials is due to an increased stability and resistance against oxidation rendering them potential candidates for other applications such as metal-ion and Li-S batteries and other electrocatalysis like oxygen evolution reaction catalysis.

Experimental sections

Detailed experimental sections can be found in the supporting information.

1. the synthesis of four kinds of nickel cobalt sulfide nanostructures; graphene oxide; nickel cobalt sulfide /S, N co-doped reduced graphene oxide hybrid materials; S, N doped graphene-

based nickel cobalt sulfide aerogel (Ni-Co-S/SNGA) and S, N co-doped graphene aerogel (SNGA).

2. Materials characterization

3. electrochemical properties testing and devices fabrication

Supporting Information
Supporting Information is available from the Wiley Online Library or from the author.

Acknowledgements
The authors thank Prof. Qiang Zhang (Tsinghua University, China), Dr. Qi Fan (Yale University, U.S.A.) and Mr. Jianmin Li (Donghua University, China) for useful discussion and suggestions and thank Dr. Sanjayan Sathasivam and Dr. Caroline E. Knapp (UCL, Department of Chemistry, U.K.) for the equipment ordering. G. J. He, M. Qiao and T. T. Zhao would like to thank the China Scholarship Council for funding. G. J. He and T. T. Zhao thank the UCL Dean's prize for the joint Ph. D scholarship.

Received: ((will be filled in by the editorial staff))
Revised: ((will be filled in by the editorial staff))
Published online: ((will be filled in by the editorial staff))

References

[1] K. S. Novoselov, A. K. Ceim, S. V. Morozov, D. Jiang, Y. Zhang, S. V. Dubonos, I. V. Grigorieva，A. A. Firsov, *Science*, **2004**, *306*, 666.

[2] C. L. A. Peigney, E. Flahaut, R. R. Bacsa, A. Rousset, *Carbon*, **2001**, *39*, 507.

[3] F. Bonaccorso, L. Colombo, G. Yu, M. Stoller, V. Tozzini, A. C. Ferrari, R. S. Ruoff, V. Pellegrini, *Science*, **2015**, *347*, 1246501.

[4] Y. Shao, M. F. El-Kady, L. J. Wang, Q. Zhang, Y. Li, H. Wang, M. F. Mousavi, R. B. Kaner, *Chem. Soc. Rev.*, **2015**, *44*, 3639.

[5] H. Chang, H. Wu, *Adv. Funct. Mater.*, **2013**, *23*, 1984.

[6] J. Yang, C. Yu, X. Fan, C. Zhao, J. Qiu, *Adv. Funct. Mater.*, **2015**, *25*, 2109.

[7] X. Wang, J. Wang, D. Wang, S. Dou, Z. Ma, J. Wu, L. Tao, A. Shen, C. Ouyang, Q. Liu, S. Wang, *Chem. Commun. (Camb)*, **2014**, *50*, 4839.

[8] Z. Chen, W. Ren, L. Gao, B. Liu, S. Pei, H. M. Cheng, *Nat. Mater.*, **2011**, *10*, 424.

[9] W. Wei, S. Yang, H. Zhou, I. Lieberwirth, X. Feng, K. Mullen, *Adv. Mater.*, **2013**, *25*, 2909.

[10] C. Zhao, C. Yu, S. Liu, J. Yang, X. Fan, H. Huang, J. Qiu, *Adv. Funct. Mater.*, **2015**, *25*, 6913.

[11] J. T. Tai, Y. C. Lai, J. H. Yang, H. C. Ho, H. F. Wang, R. M. Ho, D. H. Tsai, *Anal. Chem.*, **2015**, *87*, 3884.

[12] Y. Xu, Z. Lin, X. Zhong, X. Huang, N. O. Weiss, Y. Huang, X. Duan, *Nat. Commun.*, **2014**, *5*, 4554.

[13] L. M. Dai, L. T. Qu, H. Choi, J. B. Baek, *Chem. Rev.*, **2015**, *115*, 4823.

[14] D. Higgins, P. Zamani, A. Yu, Z. Chen, *Energy Environ. Sci.*, **2016**, *9*, 357.

[15] Z. Yu, L. Tetard, L. Zhai, J. Thomas, *Energy Environ. Sci.*, **2015**, *8*, 702.

[16] D. Bhattacharjya, A. Sinhamahapatra, J. J. Ko, J. S. Yu, *Chem. Commun. (Camb)*, **2015**, *51*, 13350.

[17] R. Zou, Z. Zhang, M. F. Yuen, M. Sun, J. Hu, C.-S. Lee, W. Zhang, *NPG Asia Mater.*, **2015**, *7*, e195.

[18] R. Zou, K. Xu, T. Wang, G. He, Q. Liu, X. Liu, Z. Zhang, J. Hu, *J. Mater. Chem. A*, **2013**, *1*, 8560.

[19] B. Yang, L. Yu, H. Yan, Y. Sun, Q. Liu, J. Liu, D. Song, S. Hu, Y. Yuan, L. Liu, J. Wang, *J. Mater. Chem. A*, **2015**, *3*, 13308.

[20] H. Hu, B. Y. Guan, X. W. Lou, *Chem*, **2016**, *1*, 102.

[21] X. Y. Yu, L. Yu, X. W. Lou, *Adv. Energy Mater.*, **2016**, *6*, 1501333.

[22] L. Yu, L. Zhang, H. B. Wu, X. W. Lou, *Angew. Chem. Int. Ed.*, **2014**, *53*, 3711.

[23] Z. Zhang, X. Wang, G. Cui, A. Zhang, X. Zhou, H. Xu, L. Gu, *Nanoscale*, **2014**, *6*, 3540.

[24] J. Wu, S. Dou, A. Shen, X. Wang, Z. Ma, C. Ouyang, S. Wang, *J. Mater. Chem. A*, **2014**, *2*, 20990.

[25] D. Kong, J. J. Cha, H. Wang, H. R. Lee, Y. Cui, *Energy Environ. Sci.*, **2013**, *6*, 3553-3558.

[26] L. Shen, J. Wang, G. Xu, H. Li, H. Dou, X. Zhang, *Adv. Energy Mater.*, **2015**, *5*, 1400977.

[27] H. Chen, L. Hu, M. Chen, Y. Yan, L. Wu, *Adv. Funct. Mater.*, **2014**, *24*, 934.

[28] L. Shen, L. Yu, H. B. Wu, X. Y. Yu, X. Zhang, X. W. Lou, *Nat. Commun.*, **2015**, *6*, 6694.

[29] R. Zou, Z. Zhang, M. F. Yuen, J. Hu, C. S. Lee, W. Zhang, *Sci. Rep.*, **2015**, *5*, 7862.

[30] H. Wang, Y. Liang, Y. Li, H. Dai, *Angew. Chem. Int. Ed. Engl.*, **2011**, *50*, 10969.

[31] C. Xia, P. Li, A. N. Gandi, U. Schwingenschlögl, H. N. Alshareef, *Chem. Mater.*, **2015**, *27*, 6482.

[32] X. Liu, X. Wang, B. Zhou, W.-C. Law, A. N. Cartwright, M. T. Swihart, *Adv. Funct. Mater.*, **2013**, *23*, 1256.

[33] W. Maneeprakorn, M. A. Malik, P. O'Brien, *J. Mater. Chem.*, **2010**, *20*, 2329.

[34] C. Yuan, B. Gao, L. Su, L. Chen, X. Zhang, *J. Electrochem. Soc.*, **2009**, *156*, A199.

[35] S. Chen, S. Qiao, *ACS Nano*, **2013**, ***7***, 10190.

[36] M. Seredych, T. J. Bandosz, *J. Mater. Chem. A*, **2013**, *1*, 11717.

[37] X. Wang, G. Li, M. H. Seo, F. M. Hassan, M. A. Hoque, Z. Chen, *Adv. Energy Mater.*, **2015**, *5*, 1501106.

[38] B. Zhao, S.-Y. Huang, T. Wang, K. Zhang, M. M. F. Yuen, J.-B. Xu, X.-Z. Fu, R. Sun, C.-P. Wong, *J. Power Sources*, **2015**, *298*, 83.

[39] Y. Gao, H. Zhao, D. Chen, C. Chen, F. Ciucci, *Carbon*, **2015**, *94*, 1028.

[40] L. Fu, Y. Chen, Z. Liu, *J. Mol. Catal. A: Chem.*, **2015**, *408*, 91.

[41] Q. Liu, Z. Wu, Z. Ma, S. Dou, J. Wu, L. Tao, X. Wang, C. Ouyang, A. Shen, S. Wang, *Electrochimi. Acta*, **2015**, *177*, 298.

[42] M. Sun, J. Tie, G. Cheng, T. Lin, S. Peng, F. Deng, F. Ye, L. Yu, *J. Mater. Chem. A*, **2015**, *3*, 1730.

[43] P. Simon, Y. Gogotsi, B. Dunn, *Science*, **2014**, *343*, 1210.

[44] J. Xiao, L. Wan, S. Yang, F. Xiao, S. Wang, *Nano Lett.*, **2014**, *14*, 831.

[45] G. He, J. Li, W. Li, B. Li, N. Noor, K. Xu, J. Hu, I. P. Parkin, *J. Mater. Chem. A*, **2015**, *3*, 14272.

[46] H. Huo, Y. Zhao, C. Xu, *J. Mater. Chem. A*, **2014**, *2*, 15111.

[47] X. Lu, M. Yu, G. Wang, Y. Tong, Y. Li, *Energy Environ. Sci.*, **2014**, ***7***, 2160.

[48] P. Yang, X. Xiao, Y. Li, Y Ding, P. Qiang, X. Tan, W. Mai, Z. Lin, W. Wu, H. Jin, P. Liu, J. Zhou, C. P. Wong,

Z. L. Wang, *ACS Nano*, **2013**, *7*, 2617.

[49] H. Zheng, T. Zhai, M. Yu, S. Xie, C. Liang, W. Zhao, S. C. I. Wang, Z. Zhang, X. Lu, *J. Mater. Chem. C*, **2013**, *1*, 225.

[50] X. Xiao, T. Ding, L. Yuan, Y. Shen, Q. Zhong, X. Zhang, Y. Cao, B. Hu, T. Zhai, L. Gong, J. Chen, Y. Tong, J. Zhou, Z. L. Wang, *Adv. Energy Mater.*, **2012**, *2*, 1328.

[51] X. Lu, M. Yu, G. Wang, T. Zhai, S. Xie, Y. Ling, Y. Tong, Y. Li, *Adv. Mater.*, **2013**, *25*, 267.

[52] V. S. Maher F. El-Kady, Sergey Dubin, R. B. Kaner, *Science*, **2012**, *335*, 1326.

[53] X. Lu, Y. Zeng, M. Yu, T. Zhai, C. Liang, S. Xie, M. S. Balogun, Y. Tong, *Adv. Mater.*, **2014**, *26*, 3148.

[54] J. Xu, Q. Wang, X. Wang, Q. Xiang, B. Liang, D. Chen, G. Shen, *ACS Nano*, **2013**, ***7***, 5453.

[55] Z. Wang, Z. Zhu, J. Qiu, S. Yang, *J. Mater. Chem. C*, **2014**, *2*, 1331.

[56] H. Gao, F. Xiao, C. B. Ching, H. Duan, *ACS Appl. Mater. Interfaces*, **2012**, *4*, 7020.

[57] H. Gao, F. Xiao, C. B. Ching, H. Duan, *ACS Appl. Mater. Interfaces*, **2012**, *4*, 2801.

[58] Q. Liu, J. Jin, J. Zhang, *ACS Appl. Mater. Interfaces*, **2013**, *5*, 5002.

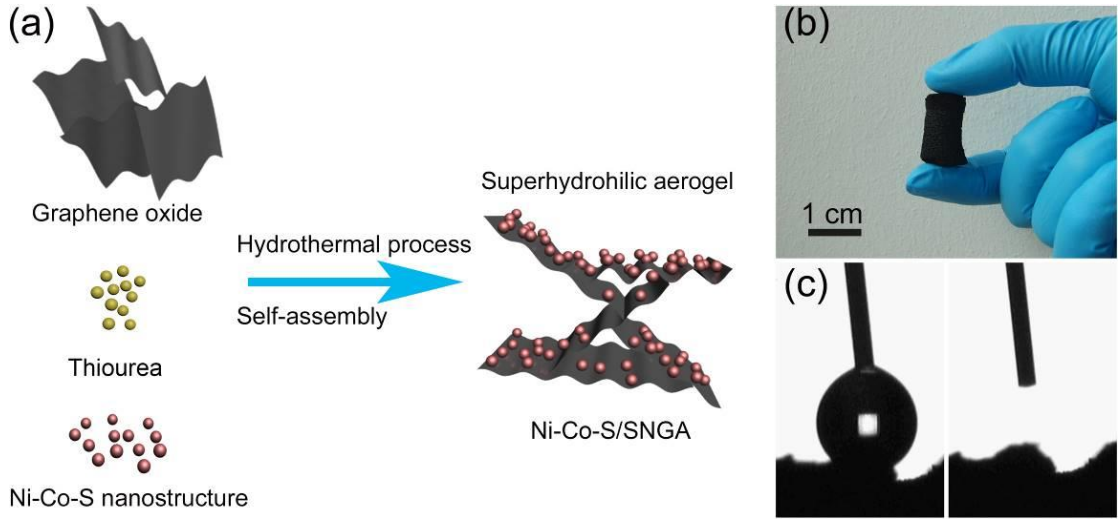

Figure 1. (a) Schematic diagram of the synthesis of Ni-Co-S/SNGA; (b) Digital camera photo of the typical aerogel sample; (c) contact angle measurements before (left) and after (right) water dropping.

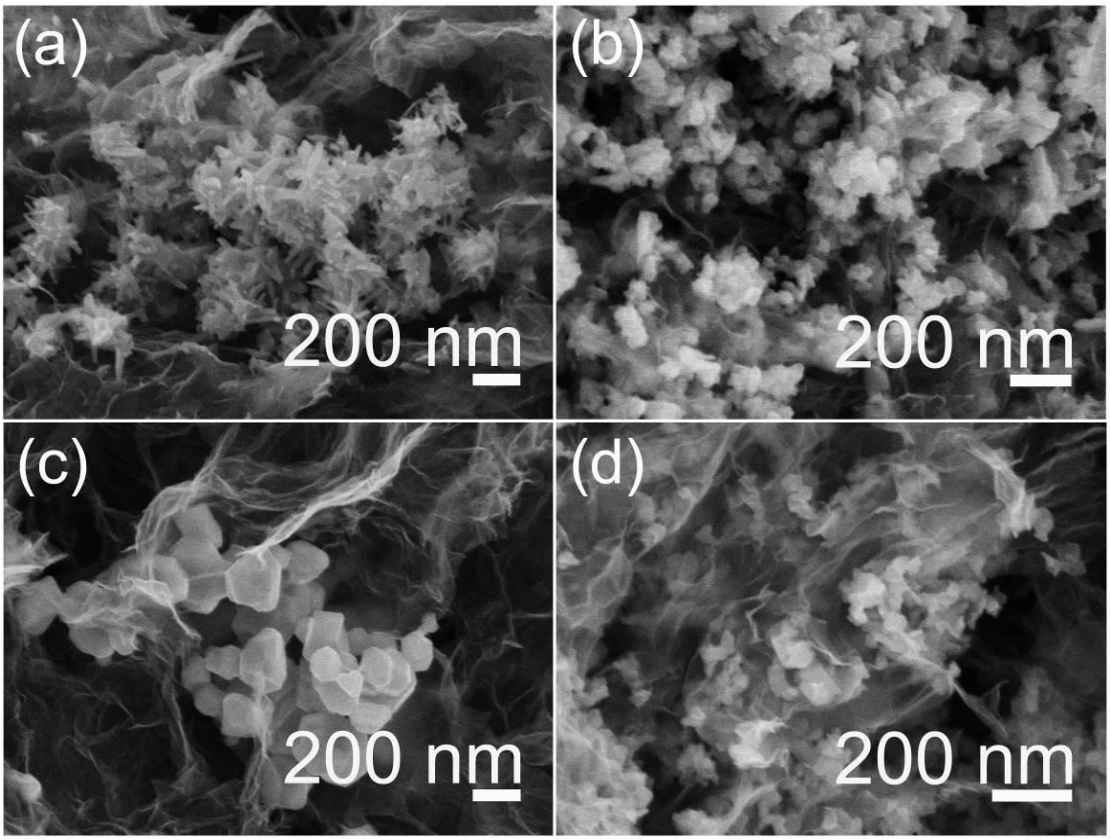

Figure 2. SEM pictures of (a) $CoNi_2S_4$/SNGA, (b) $NiCo_2S_4$/SNGA, (c) Ni-S/SNGA and (d) Co-S/SNGA, respectively.

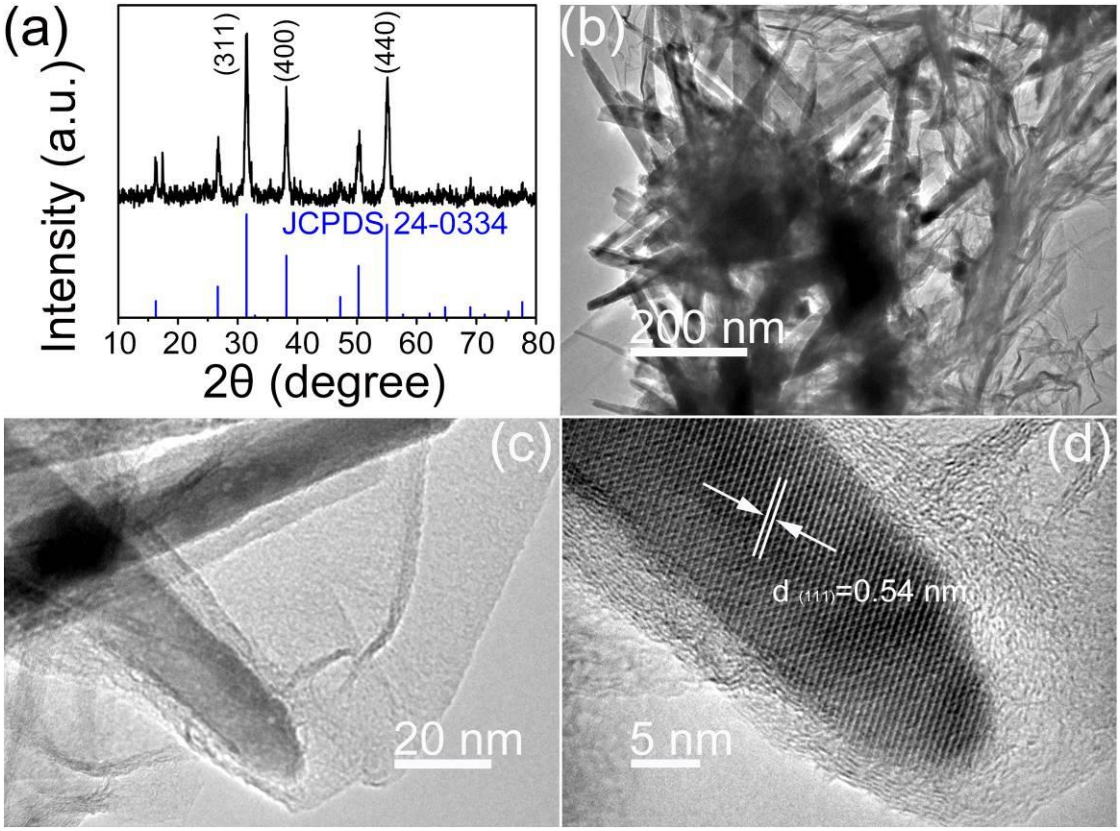

Figure 3. (a) XRD patterns of $CoNi_2S_4$/SNGA and $CoNi_2S_4$ reference pattern; (b-c) Low-, high-magnification TEM images and (d) HRTEM of $CoNi_2S_4$/SNGA.

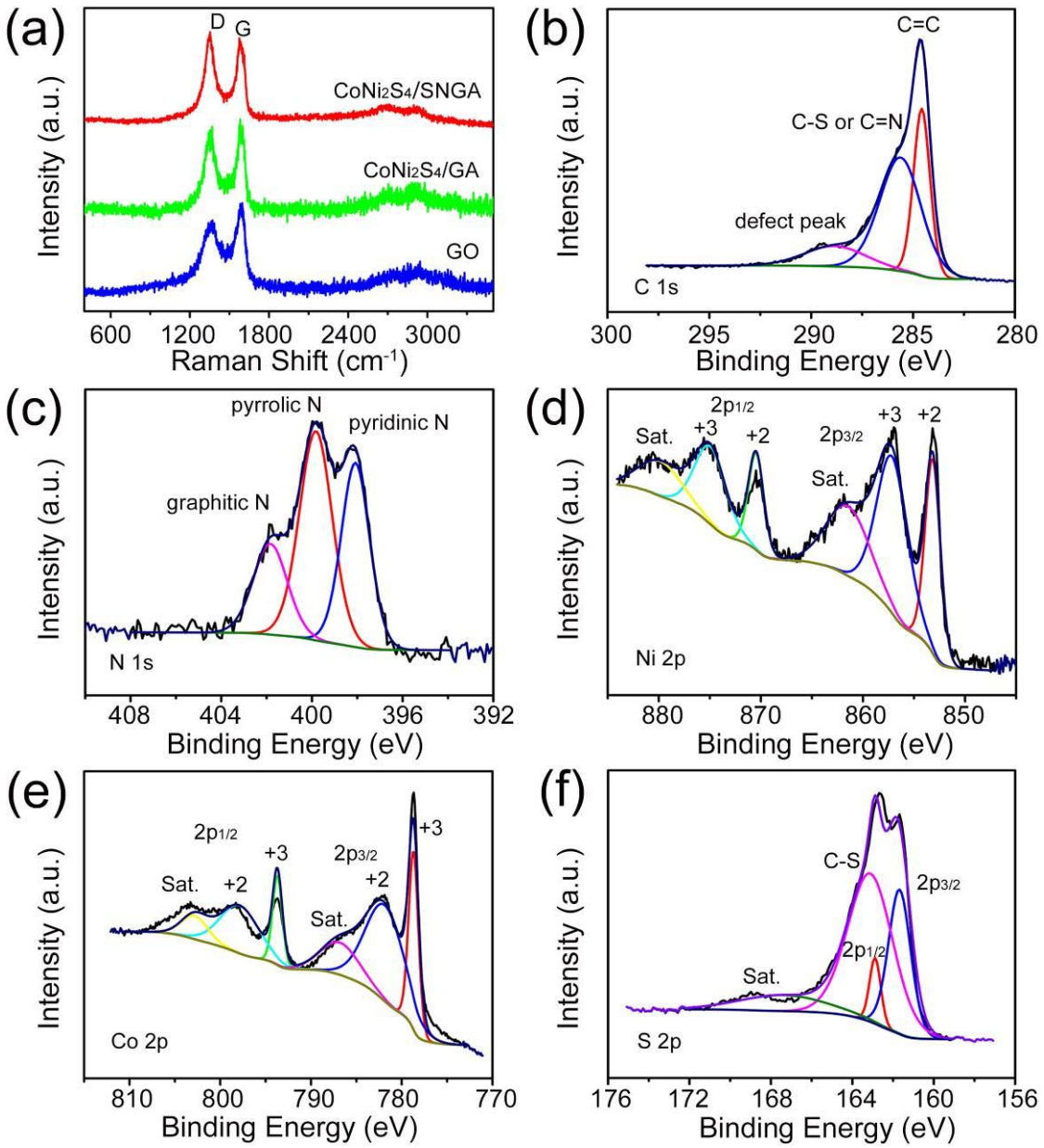

Figure 4. (a) Raman spectra of as-synthesized GO, $CoNi_2S_4$/GA and $CoNi_2S_4$/SNGA, respectively; XPS spectra of (b) C 1s, (c) N 1s, (d) Ni 2p, (e) Co 2p and (f) S 2p spectra of $CoNi_2S_4$/SNGA sample, respectively.

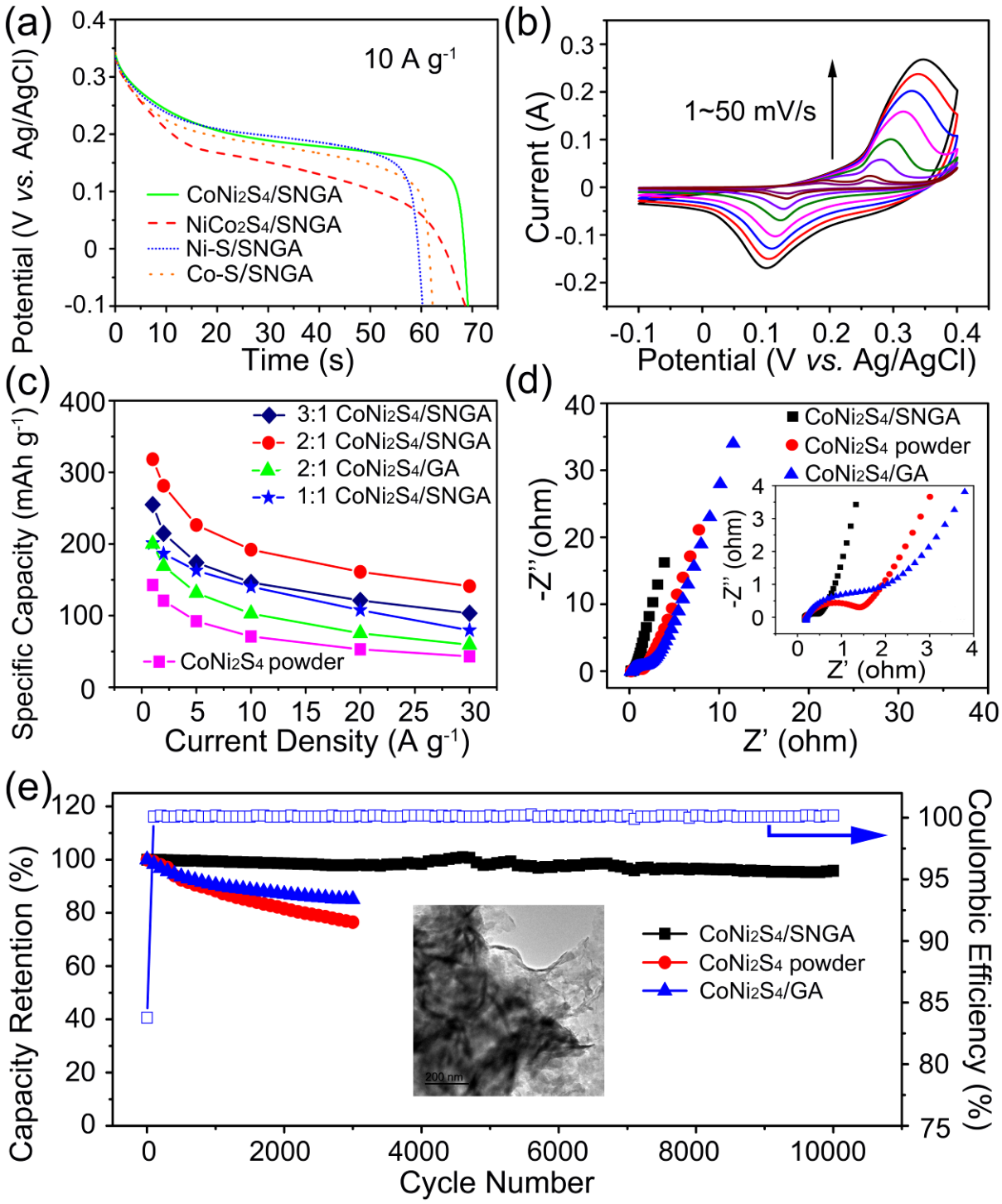

Figure 5. (a) Discharge curves of $CoNi_2S_4$/SNGA, $NiCo_2S_4$/SNGA, Ni-S/SNGA, Co-S/SNGA at the current density of 10 A g^{-1}; (b) Cyclic voltammetry curves of $CoNi_2S_4$/SNGA at the scan rate of 1~50 mV s^{-1}; (c) The comparison of specific discharge capacity for different ratios of $CoNi_2S_4$/SNGA, $CoNi_2S_4$/GA and $CoNi_2S_4$ powder samples as a function of current densities; (d) Nyquist curves of $CoNi_2S_4$/SNGA, $CoNi_2S_4$/GA and $CoNi_2S_4$ electrodes,

inset showing high-frequency parts of the EIS spectra for these samples; (e) Cycling performance of the $CoNi_2S_4$/SNGA for 10000 cycles and $CoNi_2S_4$/GA and $CoNi_2S_4$ electrodes for 3000 cycles, respectively, inset showing the TEM image of the $CoNi_2S_4$/SNGA after long-term cycling.

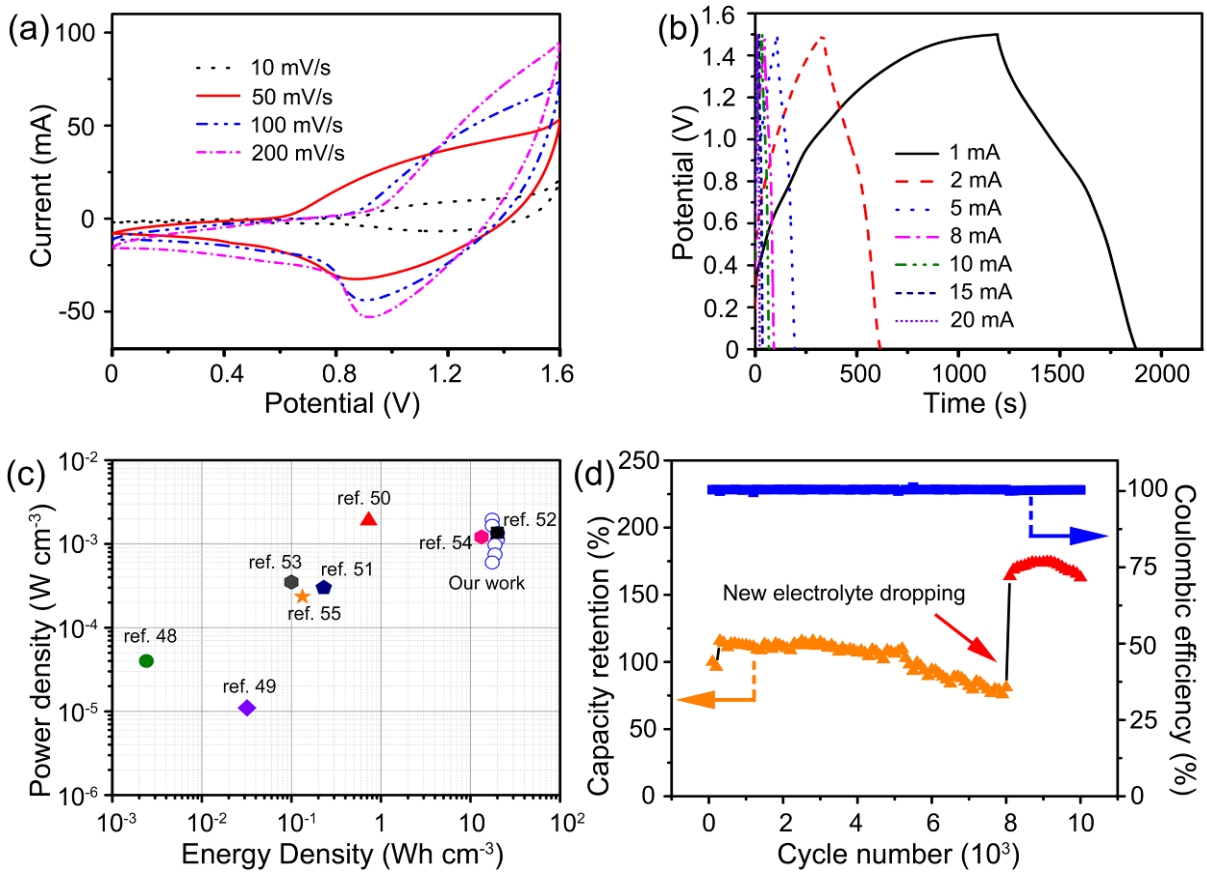

Figure 6. (a) CV curves for the hybrid battery (SNGA//$CoNi_2S_4$/SNGA) at the scan rate of 10, 50, 100 and 200 mV s^{-1}, respectively; (b) GCD curves at the current of 1, 2, 5, 8, 10 and 20 mA, respectively; (c) Ragone plot of the hybrid battery and compared with some devices values in literature; (d) Cycling performance of the devices at a current of 20 mA.

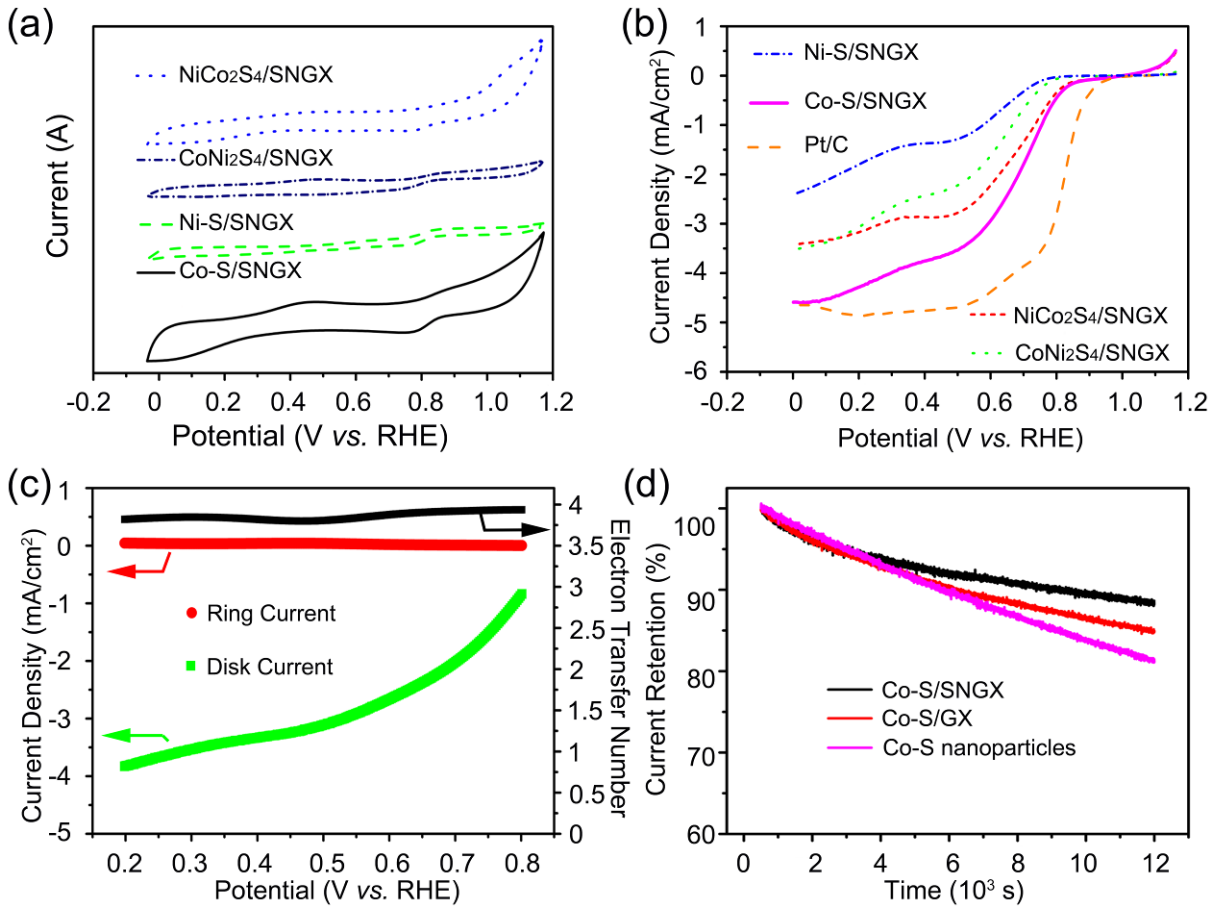

Figure 7. (a) CV curves of Ni-Co-S/SNGA in O_2-saturated 0.1 M KOH at room temperature; (b) Rotating-disk electrode (RDE) measurement of Ni-Co-S in O_2-saturated 0.1 M KOH at 1600 rpm with a sweep rate of 10 mV s^{-1}; (c) RRDE measurement of Co-S/SNGA. Two curves representing the current density on the disk (i_{disk}, green curve) and ring (i_{ring}, red curve) electrodes respectively and the electron transfer number (black curve); (d) 12000 s current-time chronoamperometric responses of Co-S/SNGA, Co-S/GA and Co-S nanostructures at a rotation rate of 1600 rpm in O_2-saturated 0.1 M KOH.

Table of Contents

Nanomaterials for energy storage and conversion applications are highly demand. However, research for highly stable electrodes/catalysts materials remains a challenge. Nickel cobalt sulfide capped in S, N co-doped graphene aerogels were developed with the aim to optimize the electrochemical performances for rechargeable alkaline battery electrodes and oxygen reduction reaction, especially the cycling performances.

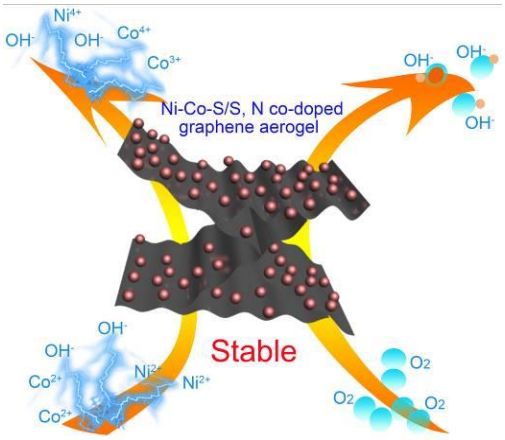

Supporting Information

S, N-co-doped Graphene-Nickel Cobalt Sulfide Aerogel: Improved Energy Storage and Electrocatalytic Performance

*Guanjie He[a], Mo Qiao[b], Wenyao Li[c], Yao Lu[a], Tingting Zhao[a], Rujia Zou[c], Bo Li[d], Jawwad A. Darr[a], Junqing Hu[c], Maria-Magdalena Titirici[b] and Ivan P. Parkin[a]**

Guanjie He, Yao Lu, Tingting Zhao, Prof. Jawwad A. Darr, Prof. Ivan P. Parkin

[a]Christopher Ingold Laboratory, Department of Chemistry, University College London, 20 Gordon Street, London WC1H 0AJ, U.K.,

E-mail:i.p.parkin@ucl.ac.uk

Mo Qiao, Prof. Maria-Magdalena Titirici

[b]School of Engineering and Materials Science/Materials Research Institute, Queen Mary University of London, Mile End Road, E14NS, London, UK.

Dr. Wenyao Li, Prof. Rujia Zou, Dr. Bo Li, Prof. Junqing Hu

[c]State Key Laboratory for Modification of Chemical Fibers and Polymer Materials, College of Materials Science and Engineering, Donghua University, Shanghai 201620, China.

Experimental parts:

Graphite powders were purchased from Hopkin & Williams Company (U.K.). Ni foams were from the Suzhou JSD foam metal Co. Ltd. (China). The glassy fiber papers were purchased from Fisher Scientific (U.K.). PVA was bought from Tokyo Chemical Industry Co., Ltd. All the other chemicals were purchased from Sigma-Aldrich (U.K.) or VWR International (U.K.) and used as received without further purification.

1. Synthesis of four different ratios of nickel cobalt sulfide nanostructures

Four 50 mL mixtures with different molar ratios of $Ni(NO_3)_2•6H_2O$ and $Co(NO_3)_2•6H_2O$ (1st beaker: $Ni(NO_3)_2•6H_2O$ (1 mmol) and $Co(NO_3)_2•6H_2O$ (2 mmol); 2nd beaker: $Ni(NO_3)_2•6H_2O$ (2 mmol) and of $Co(NO_3)_2•6H_2O$ (1 mmol); 3rd beaker: $Ni(NO_3)_2•6H_2O$ (3 mmol); 4th beaker: $Co(NO_3)_2•6H_2O$ (3 mmol) were prepared. The nickel and cobalt precursors were dissolved in deionized (DI) water (15 mL) and ethanol (20 mL) with magnetic stirring for 1 hour. Then, 1 g of thiourea was dissolved in the above solutions sequentially with another 1 hour stirring. Finally, the pH of each solution was adjusted to 8.0 using ammonium hydroxide solution (ACS reagent, 28 - 30% NH_3 basis). The solutions were transferred into 50 mL autoclaves and kept in the electric oven at 180 °C for 12 h.

2. Synthesis of graphene oxide

Graphene oxide (GO) was synthesized from graphite powder by the improved Hummer's methods as reported with a few adjustment.[1] Firstly, graphite powder (3 g) was added into the 98 % sulfuric acid (69 mL) in an 800 mL beaker with 145 r/min magnetic stirring for 1 h. After, potassium permanganate (9 g) was added into the above suspension during ~ 45 min. The beaker was then kept in a 35 °C oil bath for 2 h without stirring. The temperature of the reaction system was adjusted from 35 °C to 98 °C and DI water (138 mL) was added into the reaction system slowly and kept at 98 °C for 15 min during this process. Additional water (420 mL) together with preheated H_2O_2 (30%) (7.5 mL) was added while the color of the solution changed from dark brown to light yellow. The solution was kept at room temperature with magnetic stirring for 24 h. Subsequently, the powder was filtered and washed with HCl solution (H_2O (750 mL) and concentrated HCl (7.5 mL) to remove metal ions). The filter cake was re-dispersed in the DI water and the aggregates were removed from the dispersion by 15 min of centrifugation at 3000 rpm. Finally, the dispersion was purified by dialysis for three days to remove any salt impurities.

3. Synthesis of S, N doped graphene-based nickel cobalt sulfide aerogel (Ni-Co-S/SNGA) and S, N co-doped graphene aerogel (SNGA).

Briefly, the GO dispersion solution was adjusted to ~ 2 mg/ml. Different ratios of nickel cobalt sulfide nanoparticles (2:1 ratio is 0.14 g from step 1) were added into four beakers containing GO solution (35mL, ~ 2 mg/ml) respectively with magnetic stirring for 1 h. Thiourea (0.5 g) was added to each beaker with another 1 h magnetic stirring. At last, the above solutions were transferred to four 50 ml autoclaves and kept in the preheated oven at 180 ^{o}C for 12 h. The as-synthesized hydrogels were placed into the beakers with DI water (50 mL; Changing water every half day) for three days to remove the impurities and freeze-dried at ~ -50^{o}C for three days. SNGA were prepared by the same process without adding Ni-Co-S nanoparticles at the first step. For comparison, N-doped graphene based $CoNi_2S_4$ and S-doped graphene based $CoNi_2S_4$ were synthesized by using the same ratio with urea (0.4 g) and sodium sulphide (0.5 g) as the N and S sources, respectively.

4. Synthesis of nickel cobalt sulfide /S, N co-doped reduced graphene oxide hybrid materials

Firstly, certain amount of the (0.2 M $Co(NO_3)_2$, 0.525 mL and 0.1 M $Co(NO_3)_2$, 0.525 mL for $NiCo_2S_4$/SNrGO synthesis) aqueous solutions were added to 4 ml of GO water suspension (~ 2 mg/ml), followed by the addition of water (6 mL) and ethanol (6 mL), the PH of the solution was adjusted to ~ 8. The reaction was kept at 80 ^{o}C for 12 h with stirring. In the second step, thiourea (0.15 g) was added into reaction mixture with magnetic stirring for 1 h. Finally, the solution was transferred to a 25 ml autoclave for solvothermal treatment at 180^{o}C for 12 h.

Characterization: The morphology and microstructure of samples were characterized by scanning electron microscopy (SEM, Hitachi S-4800; SEM, JSM-6700F equipped with an

energy-dispersive X-ray spectrometer) and TEM (JEOL, JEM-2100). The phase and chemical composites were recorded using a D4 ENDEAVOR X-ray diffractometer (XRD; Cu-Ka radiation), an X-ray photoelectron spectroscopy (XPS; Thermo scientific K-alpha photoelectron spectrometer), Raman Spectroscopy (Renishaw Raman microscope spectrometer with the laser wavelength of 514.5 nm) and Attenuated Total Reflectance Fourier transform infrared spectroscopy (ATRFTIR, BRUKER, platinum-ATR). *Ex-situ* XRD for the charge and discharge processes of the alkaline battery electrodes were recorded on a STOE SEIFERT diffractometer (Mo source radiation). The mass of the materials for electrodes and active materials used for ORR test was weighed accurately by an analytical balance (Ohaus; $\delta = 0.01$ mg).

Electrochemical analysis:

Alkaline battery electrodes' performance testing. Electrochemical measurement of the as-synthesized electrodes were performed on a Gamry electrochemical workstation (Gamry Interface 1000) in a three-electrode cell with 6 M KOH as the electrolyte. A platinum foam (~ 2 cm^2) and an Ag/AgCl electrode were used as the counter and reference electrode, respectively. The active materials were pressed into Ni foams as binder-free and conductive reagent-free working electrodes. The mass of the active materials on nickel foam is ~ 2 mg (area of ~ 1 cm^2) for testing. The electrochemical impedance spectroscopy measurements were performed at open circuit potential with a sinusoidal signal over a frequency range from 100 kHz to 0.01 Hz at an amplitude of 10 mV. The specific capacity was calculated by the equation as follows:

$$C = \frac{I \times \Delta t}{m} \quad (1)$$

I is the applied galvanostatic current for the charge-discharge test (A). Δt is the discharge time (s), m is the mass of the active material (g). The values were calculated after 100 cycles of cyclic voltammetry (CV) at 50 mV s^{-1} for activation.

Hybrid battery devices fabrication and evaluation.

Electrolyte preparation: The electrolyte was prepared by mixing two kinds of solutions: a. 6 g of PVA was dissolved into 40 mL of DI water at the temperature of 90 ^{o}C, b. 20 mL of 6 M KOH water solution. The mixture was transferred to the room temperature with magnetic stirring for further use.

Devices fabrication: Hybrid batteries were fabricated by pressing the $CoNi_2S_4$/SNGA into the Ni foam (~ 1 cm^2) as the positive electrode and the SNGA into the Ni foam (~ 1 cm^2) as the negative electrode. The mass ratio of the positive to negative electrode was calculated according to the charge balance equation (Q_+=Q_-). Before fabrication, the electrodes were activated by CV tests at the scan rate of 50 mV s^{-1} in the 6 M KOH. The fabricated devices were left in the fume hood for 2 h to let the extra water evaporation and gel formation. Single device needs ~ 0.5 mL of PVA/KOH solutions. PVA was calculated as ~ 0.05 g of PVA in each device.

In order to satisfy the $Q_+ = Q_-$, the mass ratio (active materials) of two electrodes were decided by the following equation:

$$\frac{m_+}{m_-} = \frac{C_-}{C_+} \quad (2)$$

C_+ and C_- (mAh g^{-1}) are the mass specific capacity of the $CoNi_2S_4$/SNGA and SNGA, respectively. The mass ratio was calculated as *ca.* 1:7.

The specific capacity of the device (C_{device}) was calculated from the galvanostatic charge-discharge (GCD) curve as:

$$C_{device,volume} = \frac{I \times \Delta t}{V} \quad (3)$$

Where $C_{device,volumn}$ is the volumetric specific capacity based on the volume calculation of the whole device (mAh cm^{-3}). I is the applied galvanostatic current for the charge-discharge test (A). Δt is the discharge time (s) for the device. V is the total volume for the device (cm^3). The energy density (E_{volume} or E_{mass}) and the power density (P_{volume} or P_{mass}) based on the whole volume or mass of the device were calculated based on the following equation:

$$\mathrm{E} = I \int_0^{t_{max}} U_{(t)} dt \quad (4)$$

$$P_{output,max} = \frac{U^2}{4R_s} \quad (5)$$

$$R_s = \frac{U_{drop}}{2I} \quad (6)$$

$$E_{volume} \ or \ E_{mass} = \frac{E}{V_{device}} \ or \ \frac{E}{m_{device}} \quad (7)$$

$$P_{volume} \ or \ P_{mass} = \frac{P_{output,max}}{V_{device}} \ or \ \frac{P_{output,max}}{m_{device}} \quad (8)$$

Where E is the total energy from the device, t_{max} is the total discharge time, U is the voltage range of GCD test for the device (excluding the voltage drop from the beginning of the discharge curve), R_s is the internal resistance of the device, U_{drop} is the voltage drop from the discharge curve and I is the current from the galvanostatic test. P_{output}, I_{output} and R_e are the power, current and resistant of the external circuit.

The equation (5) was from:

$$I_{output} = \frac{U}{R_e + R_s} \quad (9)$$

$$P_{output} = {I_{output}}^2 R_e = \frac{U^2}{R_e + R_s} \times \frac{R_e}{R_e + R_s} = \frac{U^2}{R_e + \frac{{R_s}^2}{R_e} + 2R_s} = \frac{U^2}{\frac{(R_e - R_s)^2}{R_e} + 4R_s} \quad (10)$$

When $R_e = R_s$, the P_{output} can show the maximum value.

1 cm^2 device including: nickel foam, active materials, separator and gel electrolyte, the total mass: 0.24222 g; the total volume: 0.08 cm^3, the thickness was evaluated by the vernier caliper (Resolution: 0.02 mm).

Oxygen reduction reaction measurement. In a typical ORR performance test, the electrodes were prepared by mixing 4 mg of catalysts, 964 µL of DI water and 36 µL of nafion solution (5 % w/w). The mixture was then sonicated for ~ 40 min in the ice bath to obtain a homogeneous ink. For preparing rotating disk electrode (RDE), 5 µL of the slurry was then deposited onto the glassy carbon disk (3 mm in diameter) of RDE and dried for ~ 30 mins under room temperature in air. 14 µL of the same ink was applied to prepare for the rotating ring-disk electrode (RRDE, 5 mm in diameter). All tests were performed on electrochemical workstation (Metrohm Autolab PGSTAT204) in a standard three-electrode cell. The Ag/AgCl electrode and the platinum wire were used as the reference and the counter electrode, respectively. CV was performed in oxygen-saturated 0.10 M KOH solution at a scan rate of 100 mV s^{-1}. Linear sweep voltammograms (LSV) were obtained by rotating the electrode at 400, 800, 1200, 1600, 2000 and 2400 rpm respectively at a scan rate of 10 mV s^{-1} in oxygen-saturated 0.10 M KOH solution.

The analysis of transferred electron number per O_2 in the ORR procedure was based on：

$$n = \frac{4 I_d}{I_d + \frac{I_r}{N}} \quad (11)$$

Where I_d is the disk current, I_r is the ring current and N is current collection efficiency of the Pt ring. In our testing system, N was tested to be 0.25 from the reduction of $K_3Fe[CN]_6$. The current-time chronoamperometric responses was recorded after the first 500 s activation period for stabilizing the electrodes at the -0.45 V *vs.* Ag/AgCl at a rotation rate of 800 rpm in O_2-saturated 0.1 M KOH.

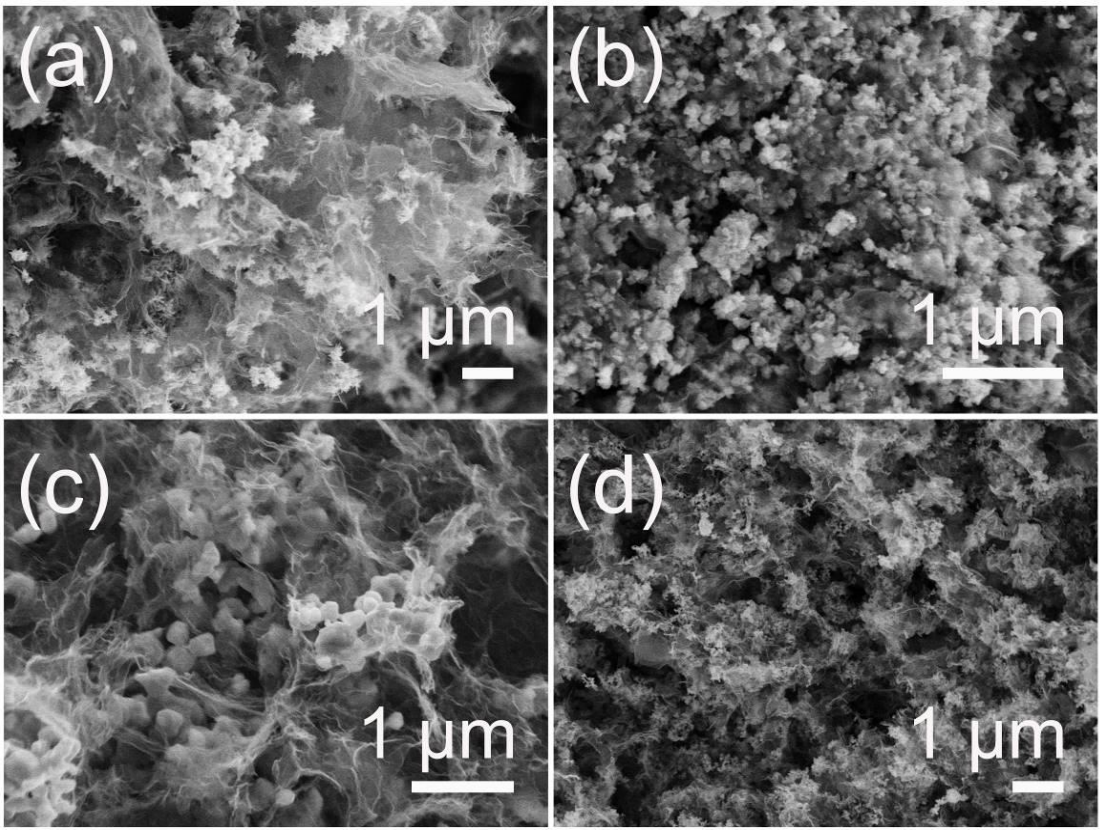

Figure. S1 (a-d) Low-magnification SEM pictures of $CoNi_2S_4$/SNGA, $NiCo_2S_4$/SNGA, Ni-S/SNGA, Co-S/SNGA, respectively.

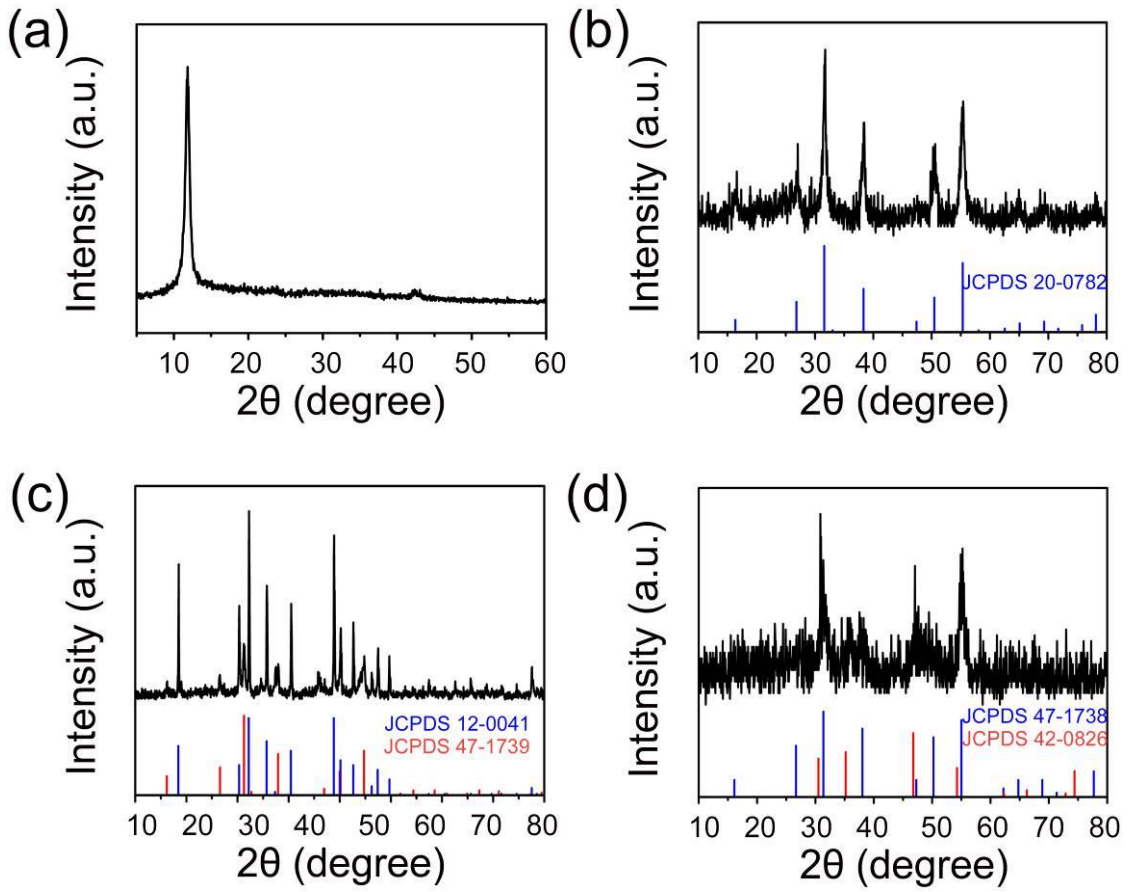

Figure. S2 XRD patterns of (a) GO; (b-d) as-synthesized Ni-Co-S/SNGA nanostructures: (b) $NiCo_2S_4$/SNGA, (c) Ni-S/SNGA and (d) Co-S/SNGA and their standard patterns, respectively.

The crystal phase of the GO and Ni-Co-S/SNGA nanostructures can be determined by XRD, The sharp peak at around $2\theta = 10.8^{o}$ corresponds to the (002) reflection of GO and disappeared in the patterns of reduced samples.[2] The $NiCo_2S_4$ nanoparticles in $NiCo_2S_4$/SNGA is the pure phase, corresponds to the Fd-3m crystal structures of standard $NiCo_2S_4$ (JCPDS no. 20-0782). By simply changing the ratio of Ni-Co-S precursors, we can obtain dual phases of Ni-S and Co-S nanoparticles, which can be indexed to the Ni_3S_4 (JCPDS no. 47-1739), NiS (JCPDS no. 12-0041) and Co_3S_4 (JCPDS no. 47-1738), $Co_{1-x}S$ (JCPDS no. 42-0826), respectively.

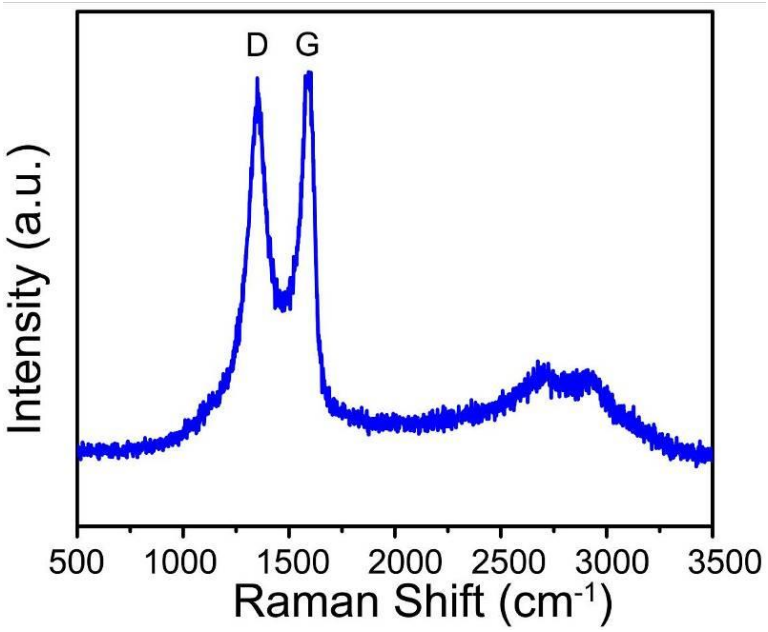

Figure. S3 Raman spectrum of the $CoNi_2S_4$/SNrGO

Table. S1 I(D)/I(G) values of the different samples.

Samples	I(D)/I(G) values
GO	0.80
$CoNi_2S_4$/SNrGO	0.91
$CoNi_2S_4$/GA	0.89
$CoNi_2S_4$/SNGA	1.05

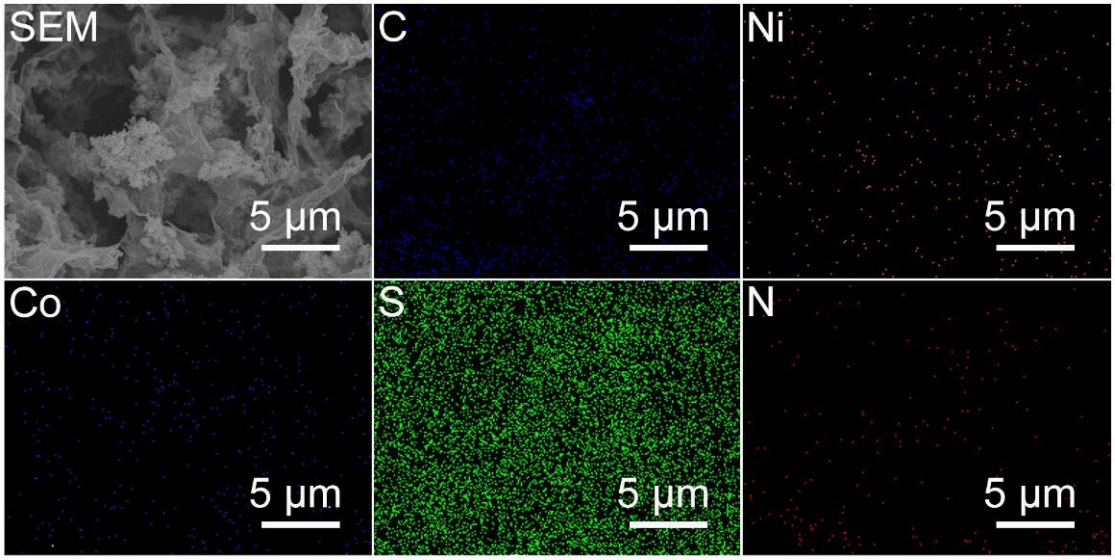

Figure. S4 Elemental mapping images of Co_2NiS_4/SNGA (C: light blue; Ni: orange; Co: dark blue; S: green and N: red)

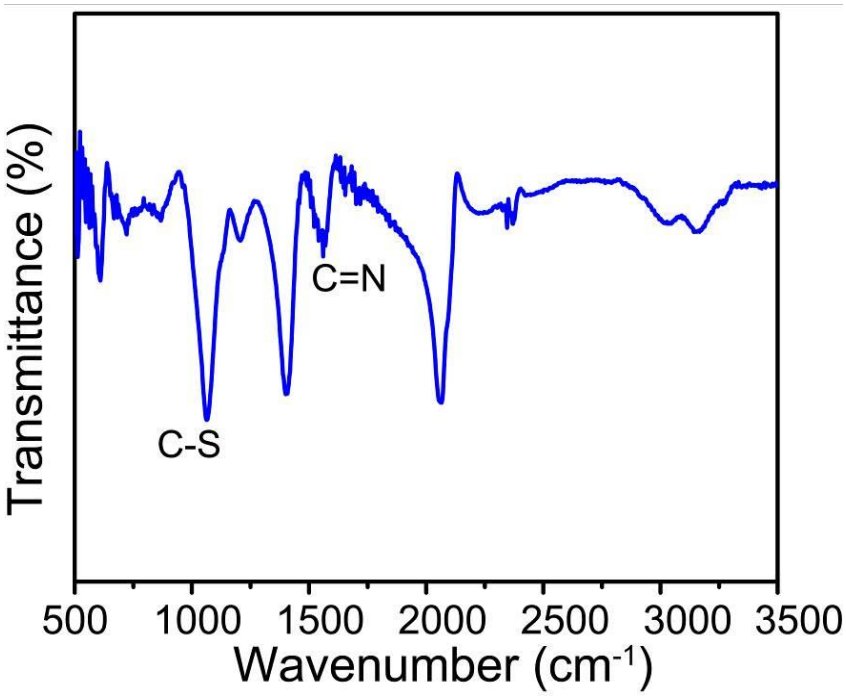

Figure. S5 FT-IR spectrum of $CoNi_2S_4$/SNGA

The C=N and C-S can be further evaluated by FTIR. The C=N streching at 1577 cm^{-1} and C-S stretching at 1068 cm^{-1} and the low intensity band at 601 cm^{-1} can be detected in the spectra. [1-3]

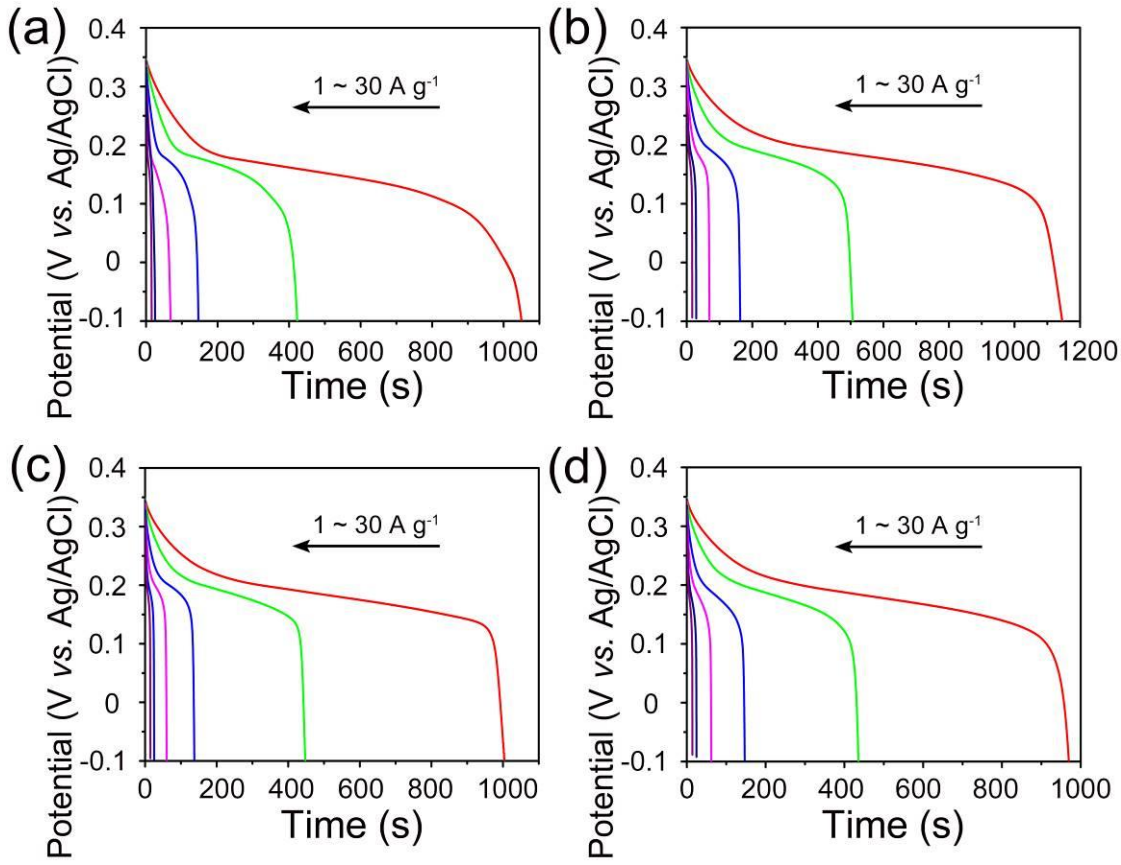

Figure. S6 Discharge curves of (a) $NiCo_2S_4$/SNGA, (b) $CoNi_2S_4$/SNGA, (c) Ni-S/SNGA, (d) Co-S/SNGA at the current densities of 1 ~ 30 A g^{-1} respectively.

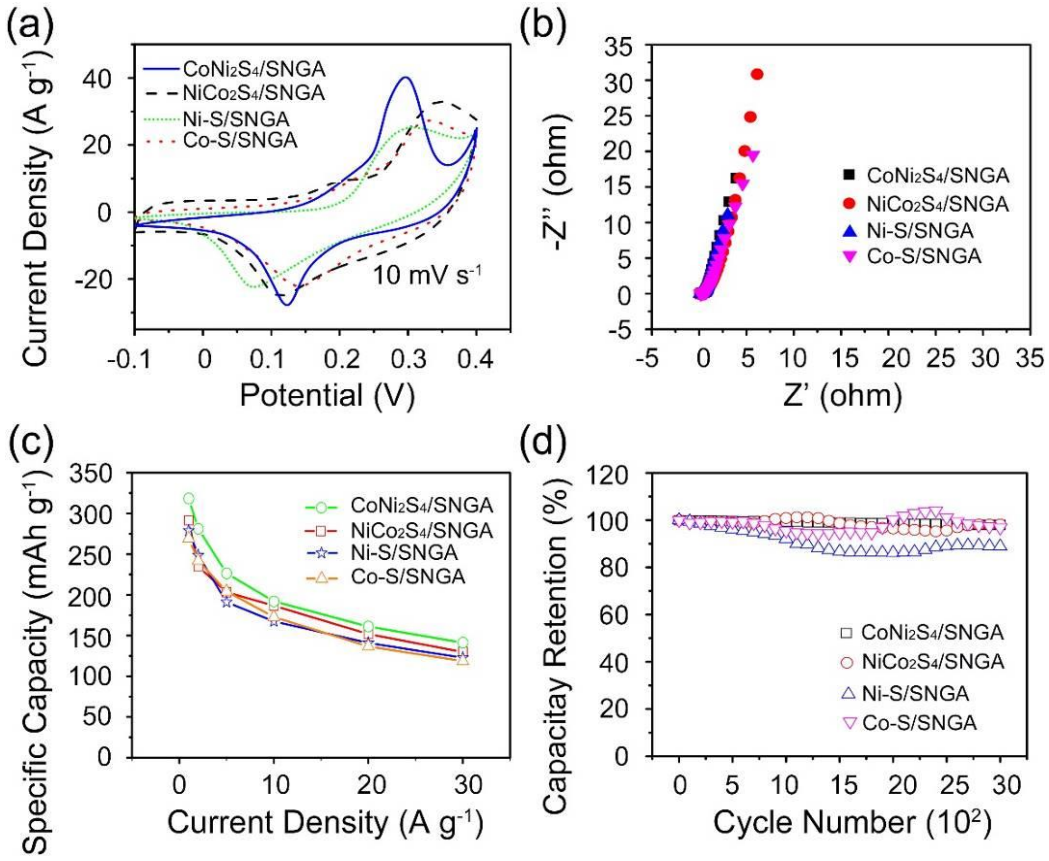

Figure. S7 (a) CV curves of $CoNi_2S_4$/SNGA, $NiCo_2S_4$/SNGA, Ni-S/SNGA and Co-S/SNGA at the scan rate of 10 mV s^{-1}, respectively; (b) Nyquist plot of the $CoNi_2S_4$/SNGA, $NiCo_2S_4$/SNGA, Ni-S/SNGA and Co-S/SNGA, respectively; (c) Rate capability of the $CoNi_2S_4$/SNGA, $NiCo_2S_4$/SNGA, Ni-S/SNGA and Co-S/SNGA at the current densities from 1~30 A g^{-1}, respectively. (d) Cycling performances of $CoNi_2S_4$/SNGA, $NiCo_2S_4$/SNGA, Ni-S/SNGA and Co-S/SNGA with the cycle numbers of 3000.

The calculations of the specific capacity were based on Figure. S4, the corresponding capacity retentions of the four kinds of samples were shown in Figure. S5 (c).

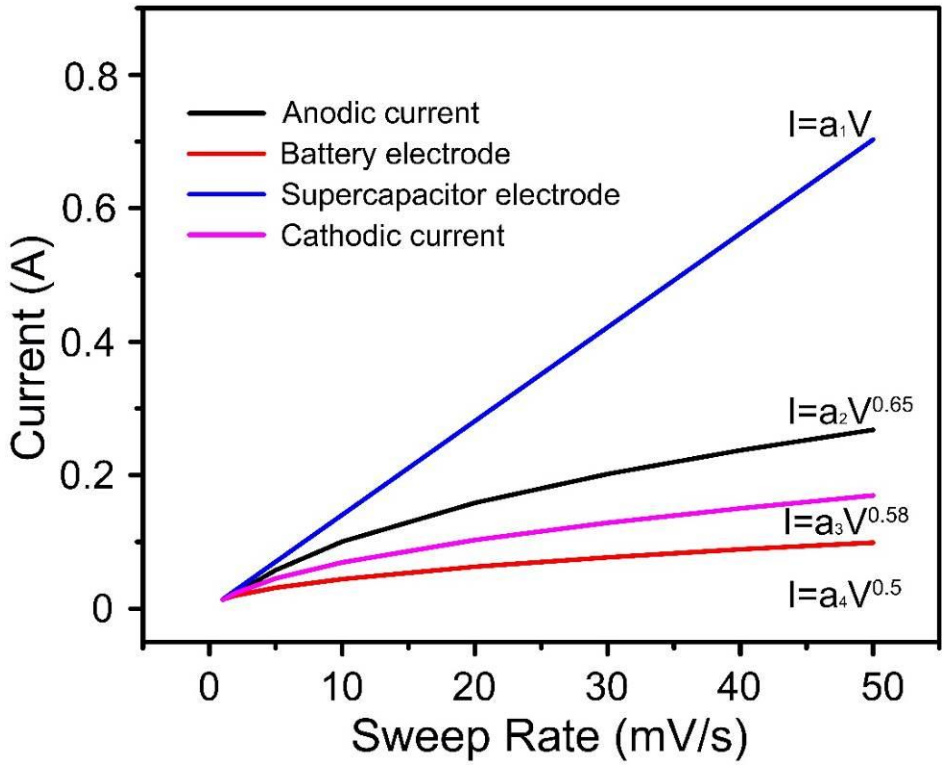

Figure. S8 The relation between peak current and the sweep rate from the CV curves of $CoNi_2S_4$/SNGA, ideal supercapacitor electrode and battery electrode, respectively.

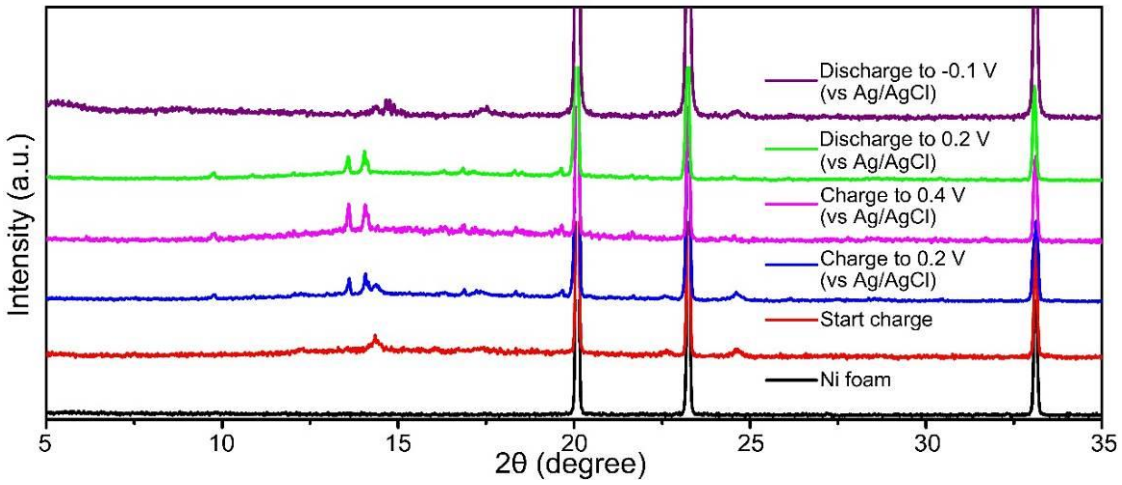

Figure. S9 *Ex-situ* XRD measurements of $CoNi_2S_4$/SNGA samples during different electrochemical steps.

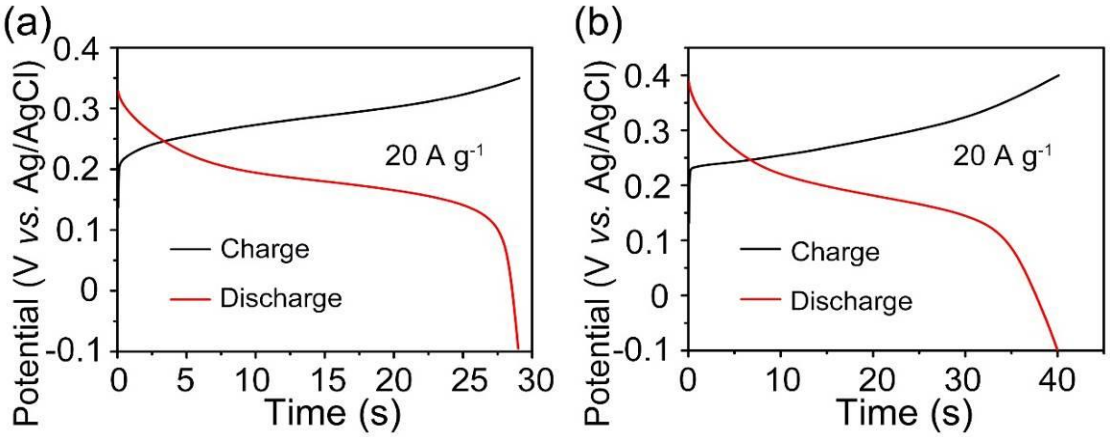

Figure. S10 GCD curves of $CoNi_2S_4$/SNGA at the current density of 20 A g^{-1} with different current window (a)-0.1~0.35 V (b) -0.1~0.4 V (*vs.* Ag/AgCl).

The calculation of the specific discharge capacity when the current density is 20 A g^{-1}:

When the voltage range is 0.45 V:

C=161.1 mAh g^{-1}

When the voltage range is 0.5 V:

C=222.1 mAh g^{-1}

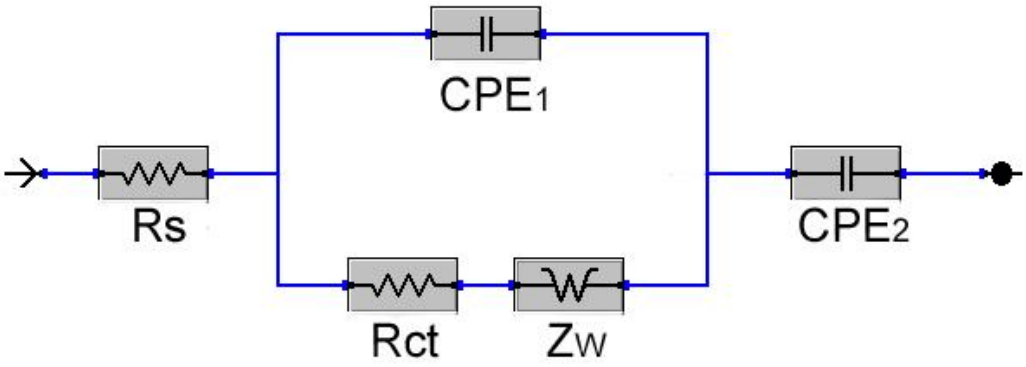

Figure. S11 Equivalent circuit of EIS for $CoNi_2S_4$/SNGA.

The parameter Rs is the inherent resistances of devices; CPE_1 and Rct are double-layer capacitance and charge transfer resistance, respectively; and Zw is the Warburg impedance related to the diffusion of OH^- ions into the bulk of the electrode. CPE_2 is caused by OH^- accumulating in the samples.

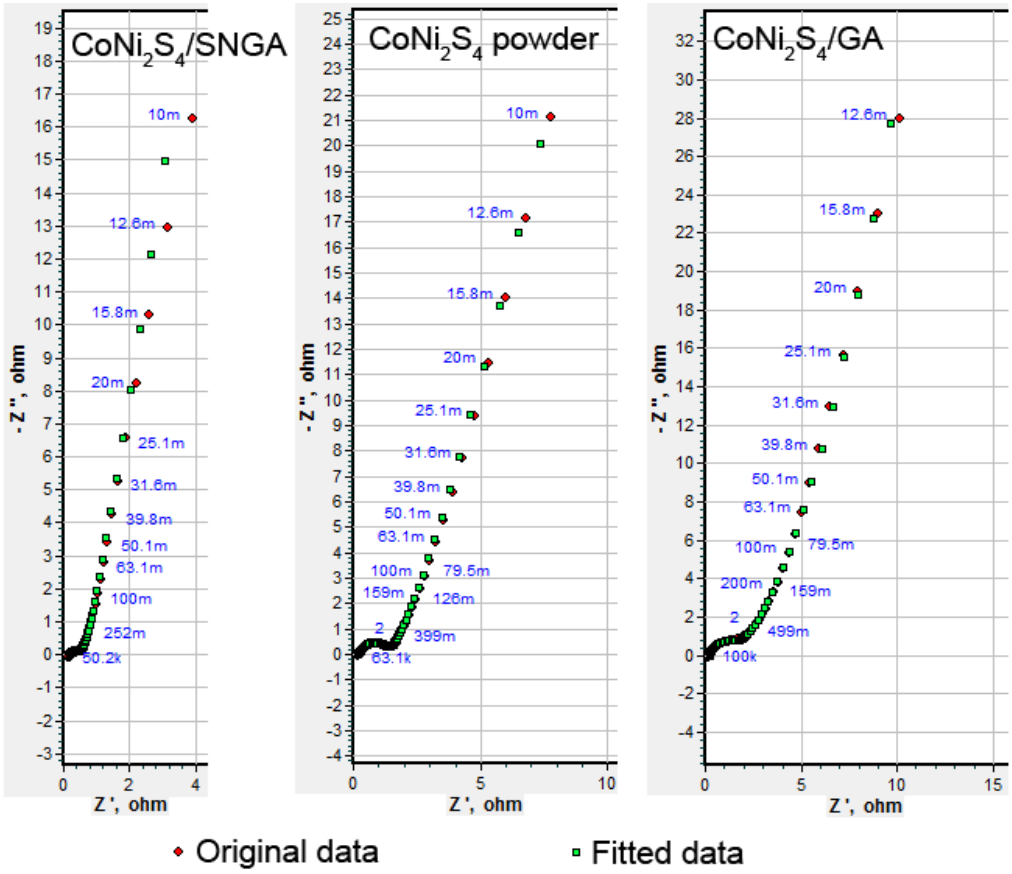

Figure. S12 Fitted EIS spectra for $CoNi_2S_4$/SNGA, $CoNi_2S_4$/GA and $CoNi_2S_4$ powder samples, respectively.

Table. S2 Comparison of rechargeable battery electrode performances of $CoNi_2S_4$/SNGA with some representative nickel/cobalt sulfide-based materials in the literature

nickel/cobalt sulfide-based materials	Specific capacity (mAh g^{-1})	Stability	Mass loading (mg cm^{-2})	References
$CoNi_2S_4$/SNGA	318.3 (1 A g^{-1})	~ 95.8% 10000 cycles	~ 2	Our work
Edge site-enriched nickel–cobalt sulfide into graphene frameworks	~ 194.8 (1 A g^{-1})	~ 90 % 8000 cycles	~ 3-3.5	[6]
CoS nanowire@$NiCo_2S_4$ nanosheet arrays	375.5 (10 mA cm^{-2})	~ 71.7 % 3000 cycles	~ 2	[7]
$CoNi_2S_4$ nanosheet arrays supported on nickel foams	363.3 (5 mA cm^{-2})	~ 78 % 3000 cycles	~ 2	[8]

Vapor-phase atomic layer deposition of Co_9S_8	205.6 (3 A g^{-1})	~ 94.4 % 2000 cycles	Not reported	[9]
$NiCo_2S_4$ nanosheets grown on nitrogen-doped carbon foams	205.2 (2 A g^{-1})	~ 90.4 % 2000 cycles	~ 2.3	[10]
Nickel cobalt sulfide ball-in-ball hollow spheres	158.3 (1 A g^{-1})	~ 87 % 2000 cycles	~ 5	[11]
$NiCo_2S_4$ nanoprisms	124.3 (1 A g^{-1})	~ 85.7 % 1500 cycles	~ 1	[12]
NiS_2 nanocube	77.2 (1.25 A g^{-1})	~ 93.4 % 3000 cycles	~ 2	[13]

*Specific capacity were calculated from specific capacitance and the voltage range in the references

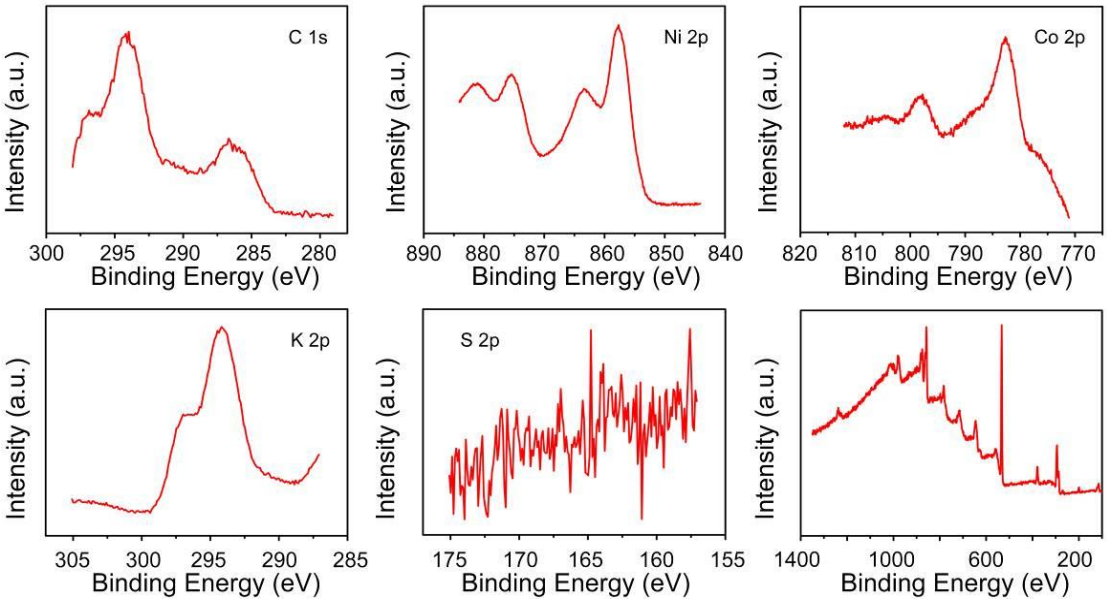

Figure. S13 XPS spectra of high-resolution of C 1s, Ni 2p, Co 2p, K 2p, S 2p and the survey spectra from $CoNi_2S_4$/GA samples after 3000 GCD cycles.

The peaks at ~ 284.8, ~ 286.3 and ~ 289.4 eV are due to the chemical state of C-C, C-O and C=O respectively. Two new peaks can be detected obviously at 293.0 and 295.8 eV after long-term cycling, which can be corresponded to the K 2p3/2 peak from the KOH electrolyte.

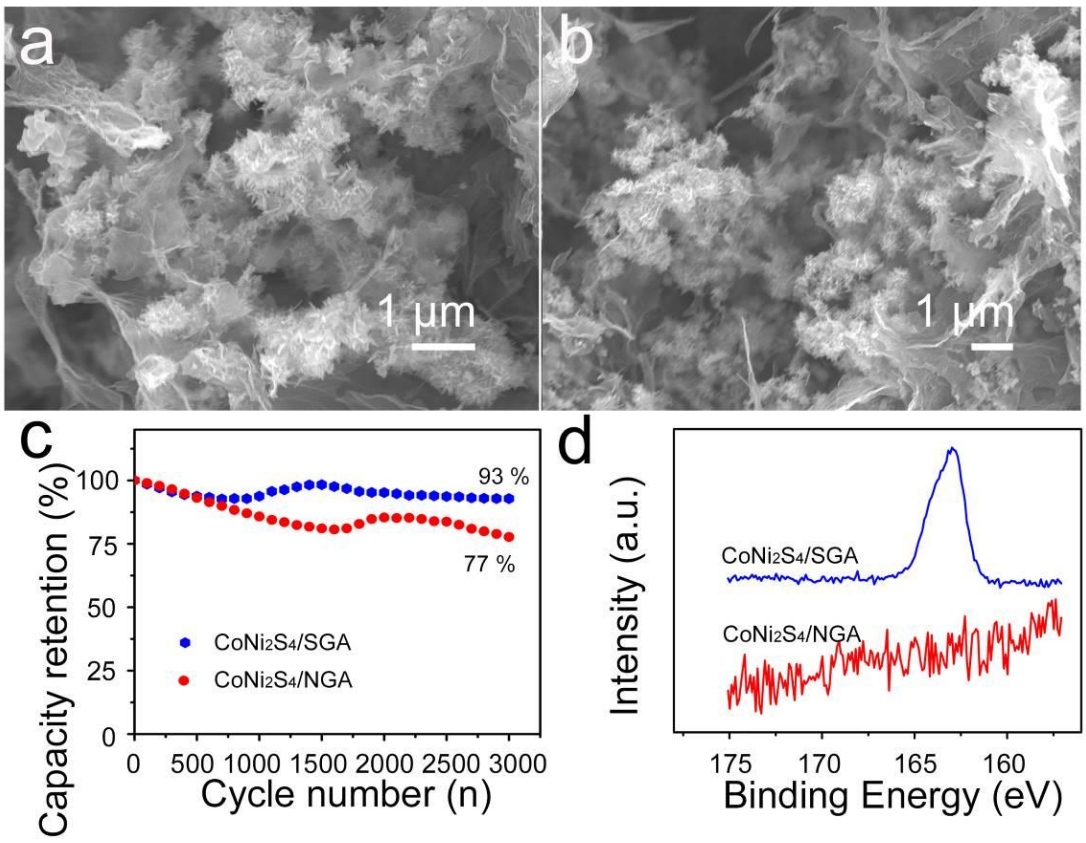

Figure. S14 (a, b) SEM images of $CoNi_2S_4$/NGA and $CoNi_2S_4$/SGA, respectively; (c) Stability test of the $CoNi_2S_4$/NGA and $CoNi_2S_4$/SGA for rechargeable alkaline battery electrodes in three electrode testing system; (d) S 2p spectra of $CoNi_2S_4$/NGA and $CoNi_2S_4$/SGA after cycling.

As can be seen from the SEM images, single doping of the graphene aerogels made almost no difference compared with co-doped graphene aerogels. The stability tests and the XPS data of S 2p proved the conclusions of the purpose of the N and S atoms.

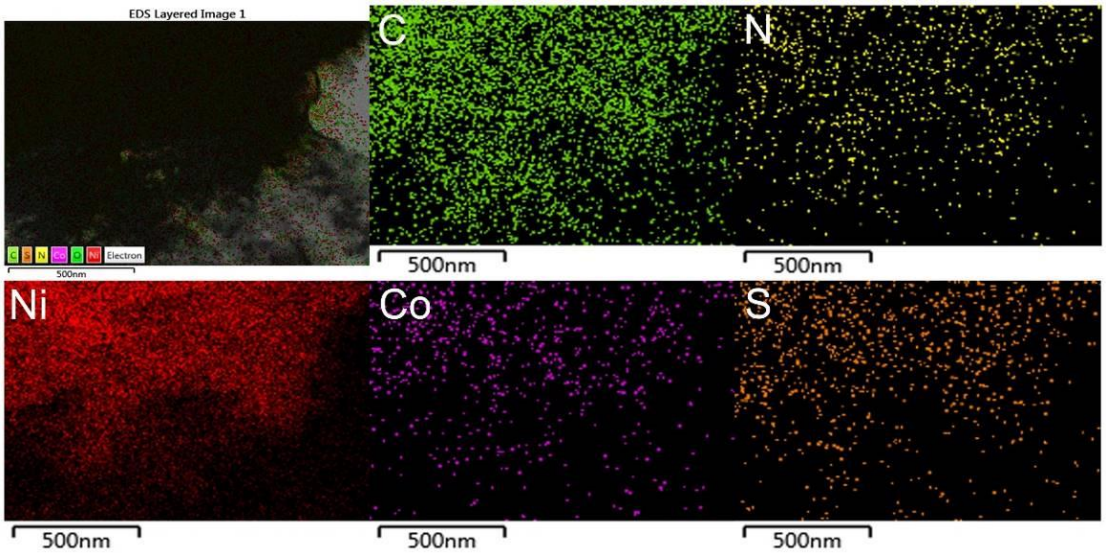

Figure. S15 TEM-EDS mapping images of the $CoNi_2S_4$/SNGA samples after 10000 GCD cycles.

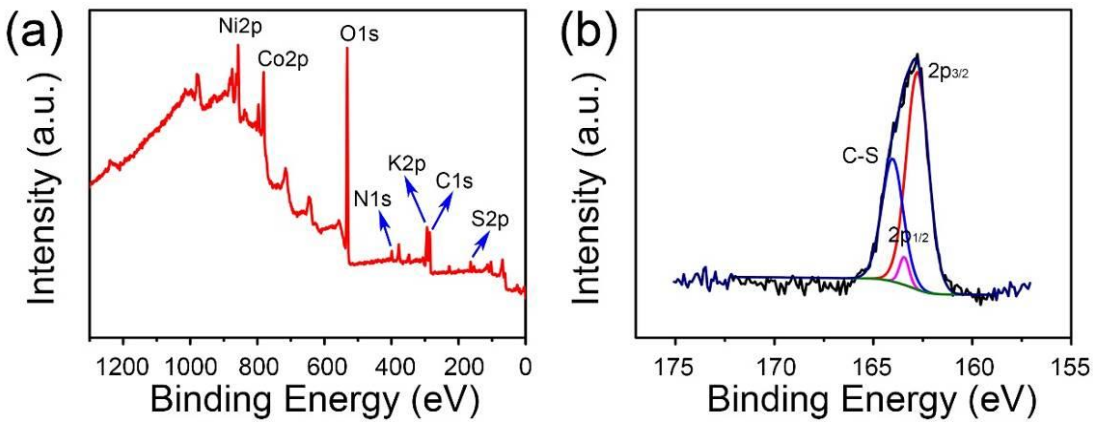

Figure. S16 XPS spectra of (a) survey and (b) high-resolution of S 2p from $CoNi_2S_4$/SNGA samples after 10000 GCD cycles.

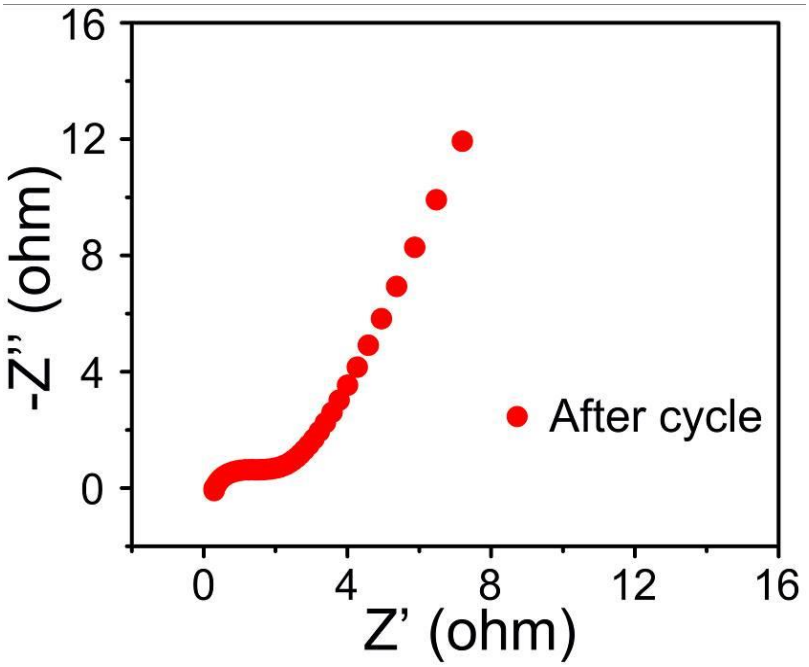

Figure. S17 EIS spectra of $CoNi_2S_4$/SNGA electrodes after 10000 GCD cycles.

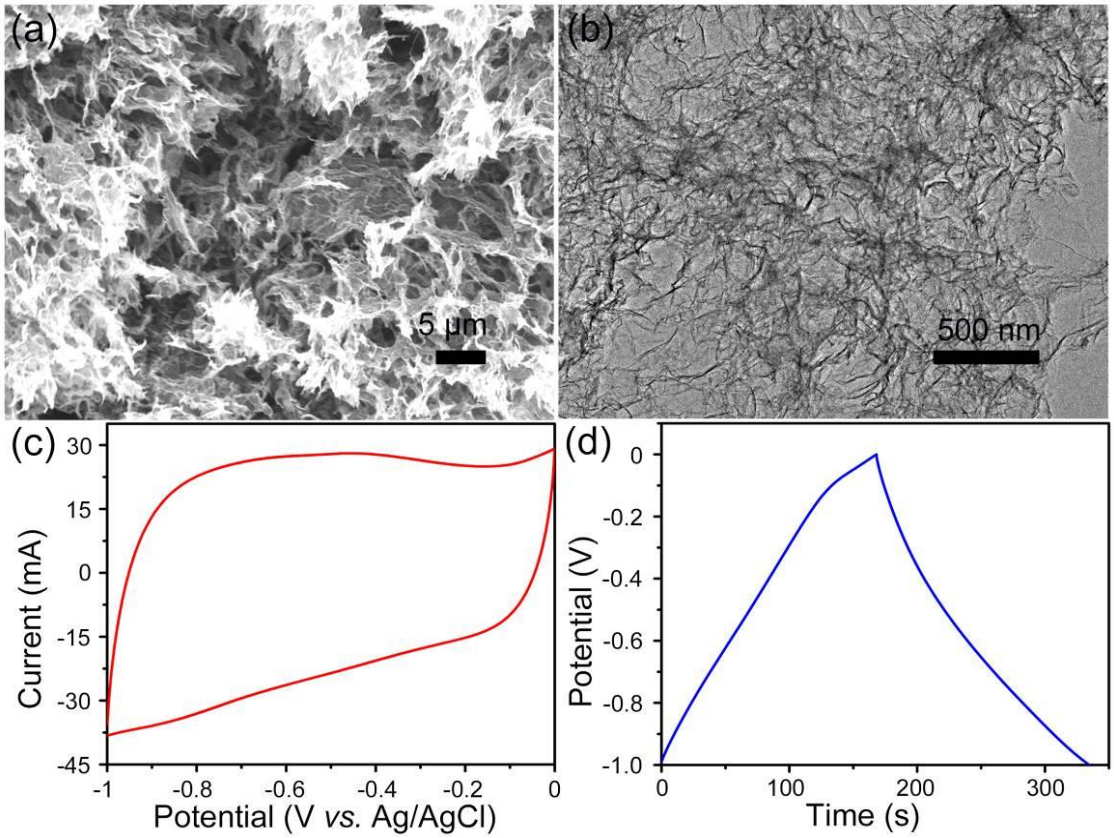

Figure. S18 (a), (b) SEM and TEM images of the SNGA, respectively; (c) CV curve of the SNGA electrode at the scan rate of 100 mV s^{-1}; (d) GCD curve of the SNGA at the current density of 1 A g^{-1}.

The calculation of the specific capacity of the SNGA is 46.2 mAh g^{-1} (specific capacitance: 166.4 F g^{-1}). According to the charge balance equation, the mass ratio of two electrodes is *ca.* 1: 7.

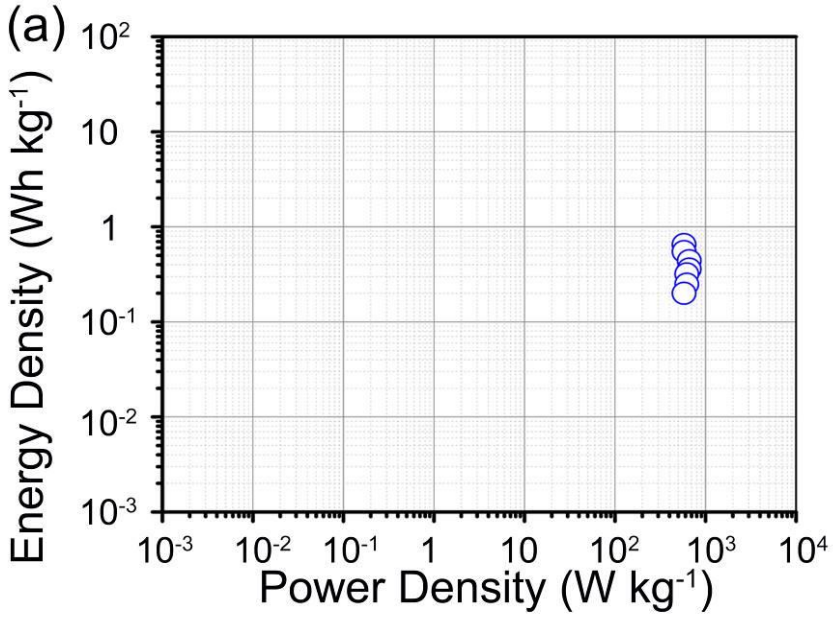

Figure. S19 Ragone plot of the device based on the total mass value.

Table. S3 Comparison of gel electrolytes and stability performances of solid-state devices from the literature with the solid-state battery in our work (SNGA//$CoNi_2S_4$/SNGA)

Solid-state devices	Gel electrolyte	Capacity retention	References
SNGA//$CoNi_2S_4$/SNGA AD	KOH/PVA gel	84 % 8000 cycles	Our work
Co_9S_8//Co_3O_4@RuO_2 AD	KOH/PVA gel	90.2 % 2000 cycles	[14]
SWCNTs//RuO_2 AD	H_3PO_4/PVA gel	~ 70 % 1000 cycles	[15]
WO_{3-x}/MoO_{3-x}//PANI/carbon fabric AD	H_3PO_4/PVA gel	75 % 10000 cycles	[16]
PPy/CNTs SD	H_3PO_4/PVA gel	73.8 % 10000 cycles	[17]

β-$Ni(OH)_2$/graphene SD	KOH/PVA gel	No detailed value 500 cycles	[18]
RuO_2/IL-CMG//IL-CMG AD	H_2SO_4/PVA gel	95 % 2000 cycles	[19]
$NiCo_2O_4$@PPy//AC AD	KOH/PVA gel	89.2 % 5000 cycles	[20]
PANI-ZIF-67 AD	H_2SO_4/PVA gel	80 % 2000 cycles	[21]

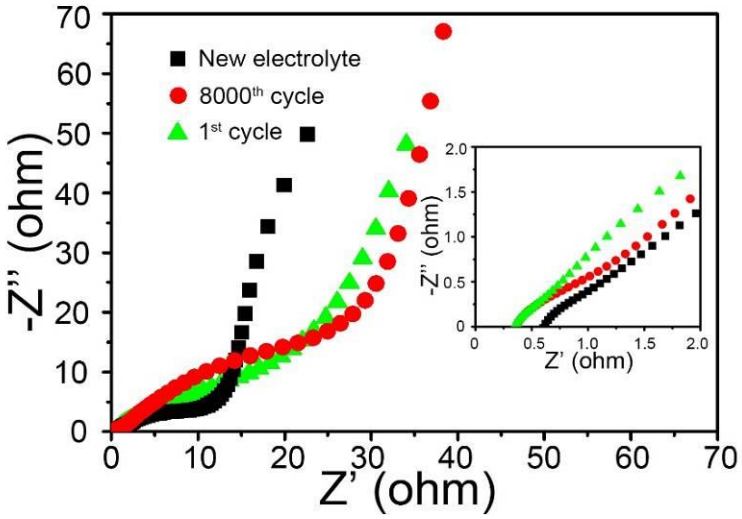

Figure. S20 EIS spectra before, after the cycling and when the new electrolyte dropping on the device.

In designing of new electrolyte dropping experiment, we wanted to verify the performances decline was mainly due to further water evaporation which inhibits the charge transfer and increases the Warburg resistance. With the addition of further electrolyte, it's obvious the inherent resistances of devices increased slightly which can be detected in the high frequency range.

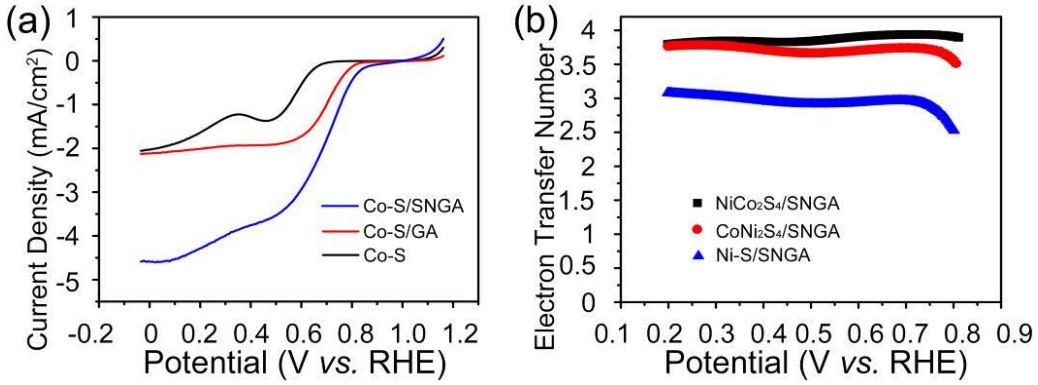

Figure. S21 (a) LSV spectra of the Co-S/SNGA, Co-S/GA and Co-S nanostructures at the rotation rate of 1600 rpm in O_2-saturated 0.1 M KOH, (b) electron transfer number of the $NiCo_2S_4$/SNGA, $CoNi_2S_4$/SNGA, Ni-S/SNGA calculated based on the RRDE value.

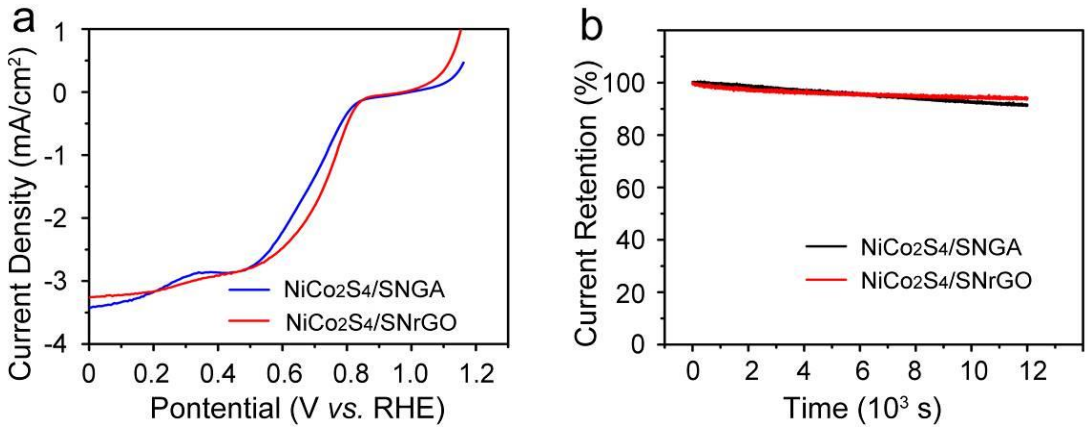

Figure. S22 (a) Rotating-disk electrode (RDE) measurements of $NiCo_2S_4$/SNGA and $NiCo_2S_4$/SNrGO in O_2-saturated 0.1 M KOH at 1600 rpm with a sweep rate of 10 mV s^{-1} (b) 12000 s of current-time chronoamperometric responses.

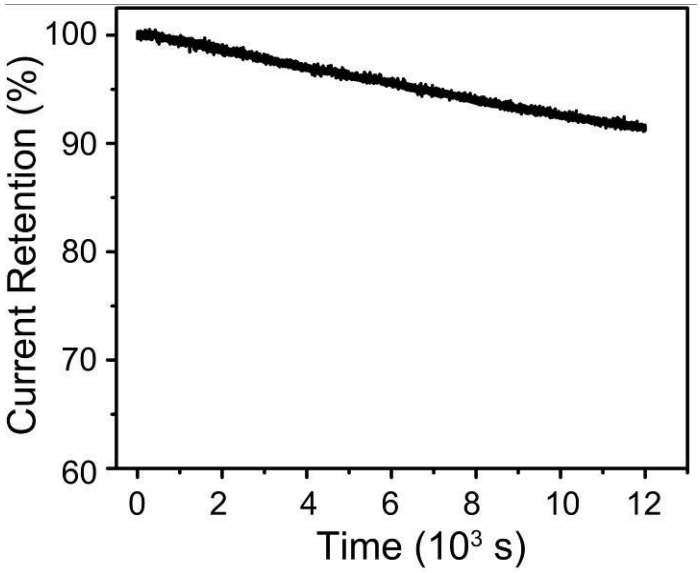

Figure. S23 Current−time chronoamperometric responses of $NiCo_2S_4$/SNGA at a rotation rate of 800 rpm for 12000 s in O_2-saturated 0.1 M KOH.

References

[1] Y. Xu, Z. Lin, X. Zhong, X. Huang, N. O. Weiss, Y. Huang, X. Duan, *Nat. Commun.*, **2014**, *5*, 4554.

[2] Y. Shao, H. Wang, Q. Zhang, Y. Li, *NPG Asia Mater.*, **2014**, *6*, e119.

[3]. F. Kanumfre, E. M. de Lima, G. Scheidt, P. I. B. Carneiro and N. D. Rosso, *J. Braz. Chem. Soc.*, **2010**, *21*, 800.

[4]. M. S. S. Babu, P.G. Krishna, K. H. Reddy and G. H. P. Chil, *Chem. Soc.*, **2009**, *54*, 339.

[5]. H. Liao, S. Chen and D. Liu, Macromolecules, **2009**, *42*, 6558.

[6] J. Yang, C. Yu, X. Fan, S. Liang, S. Li, H. Huang, Z. Ling, C. Hao, J. Qiu, *Energy Environ. Sci.*, **2016**, DOI: 10.1039/c5ee03633j.

[7] W. Zeng, G. Zhang, X. Wu, K. Zhang, H. Zhang, S. Hou, C. Li, T. Wang, H. Duan, *J. Mater. Chem. A*, **2015**, *3*, 24033.

[8] W. Hu, R. Chen, W. Xie, L. Zou, N. Qin, D. Bao, *ACS Appl. Mater. Interfaces*, **2014**, *6*, 19318.

[9] H. Li, Y. Gao, Y. Shao, Y. Su, X. Wang, *Nano Lett.*, **2015**, *15*, 6689.

[10] L. Shen, J. Wang, G. Xu, H. Li, H. Dou, X. Zhang, *Adv. Energy Mater.*, **2015**, *5*, 1400977.

[11] L. Shen, L. Yu, H. B. Wu, X. Y. Yu, X. Zhang, X. W. Lou, *Nat. Commun.*, **2015**, *6*, 6694.

[12] L. Yu, L. Zhang, H. B. Wu, X. W. Lou, *Angew. Chem. Int. Ed.*, **2014**, *53*, 3711.

[13] H. Pang, C. Z. Wei, X. X. Li, G. C. Li, Y. H. Ma, S. J. Li, J. Chen, J. S. Zhang, *Sci. Rep.*, **2014**, *4*, 3577.

[14] J. Xu, Q. Wang, X. Wang, Q. Xiang, B. Liang, D. Chen, G. Shen, *ACS Nano*, **2013**, *7*, 5453.

[15] P. Chen, H. Chen, J. Qiu, C. Zhou, *Nano Res.*, **2010**, *3*, 594.

[16] X. Xiao, T. Ding, L. Yuan, Y. Shen, Q. Zhong, X. Zhang, Y. Cao, B. Hu, T. Zhai, L. Gong, J. Chen, Y. Tong, J. Zhou, Z. L. Wang, *Adv. Energy Mater.*, **2012**, *2*, 1328.

[17] H. Lin, L. Li., J. Ren, Z. Cai, L. Qiu, Z. Yang, H. Peng, *Sci. Rep.*, **2013**, *3*, 1353.

[18] J. Xie, X. Sun, N. Zhang, K. Xu, M. Zhou, X. Yie, *Nano Energy*, **2013**, *2*, 65.

[19] B. G. Choi, S. Chang, H. Kang, C. P. Park, H. J. Kim, W. H. Hong, S. Lee, Y. S. Huh, *Nanoscale*, **2012**, *4*, 4983.

[20] D. Kong, W. Ren, C. Cheng, Y. Wang, Z. Huang, H. Y. Yang, *ACS Appl. Mater. Interfaces*, **2015**, *7*, 21334.

[21] L. Wang, X. Feng, L. Ren, Q. Piao, J. Zhong, Y. Wang, H. Li, Y. Chen, B. Wang, *J. Am. Chem. Soc.*, **2015**, *137*, 4920.